A DISTRIBUTED-SOURCE APPROACH TO MODELLING THE SPATIAL DISTRIBUTION OF MM INTENSITIES RESULTING FROM LARGE CRUSTAL NEW ZEALAND EARTHQUAKES

D. J. Dowrick[1] and D. A. Rhoades[2]

ABSTRACT

This paper presents a new approach to modelling the spatial distribution of intensities in crustal earthquakes, using a distributed source. The source is represented by one or two rectangular fault rupture planes of chosen dip, discretised into small rectangles each with its own share of the total seismic moment, and modelling chosen distributions of asperities. The Modified Mercalli (MM) intensity of shaking is represented by isoseismals. Comparisons are made with the actual isoseismals (particularly of intensities MM9 and MM10) of selected large historical crustal New Zealand earthquakes and those predicted by the simpler models of Dowrick & Rhoades (2005). Important differences and insights are found regarding near-source spatial distributions of ground shaking of shallow earthquakes with rupture length greater than about 28 km (M_w > 6.8) with any dip, and for M_w > c. 5.5 with dip < 60º. The influence of asperities relative to that of non-asperities is seen as modest near-fault increases in intensity. The new model can be applied to planar or biplanar fault ruptures of any length, width and dip. In the absence of isoseismal data on large earthquakes with normal focal mechanisms the current model is only verified for use on strike-slip and reverse events. A new concept, *seismic-source intensity*, is introduced and utilized.

The new model can also be applied to earthquakes in other regions of the world with adjustments for local attenuation rates as necessary.

1 INTRODUCTION

In assessments of earthquake shaking hazard, it is the larger earthquake sources that contribute the most. But in strong-motion and intensity-of-shaking data sets, observations close to the sources of the larger earthquakes tend to be only a small proportion of the total data. Therefore, these near-to-large-source data do not to have much influence on the fitting of attenuation models. Rather, the way in which distance from the source is modelled largely determines the fit to these data.

The predictions of strength or intensity of shaking at a given site with respect to the source of an earthquake using normal empirical attenuation models are currently of two types:

- Strong-motion (SM) attenuation models based on the shortest distance between the site and the causative fault rupture surface, or its projection onto the horizontal ground surface, and
- Modified Mercalli (MM) intensity attenuation models. Here we discuss only that of Dowrick & Rhoades (2005) (D&R 2005) which models attenuation from a point source in two directions at right angles, i.e. along-strike and strike-normal.

These two methods respectively result in racetrack shaped iso-SM lines and elliptical isoseismals. Particular concerns are establishing and modelling the spatial distribution of shaking/damage near the source of larger shallow earthquakes, and avoiding the artificial distortions (in both the near and the far field) caused by measuring distance from either a single point or the nearest point on a fault surface. The robustness of our modelling is reasonably strong because we have near-source data (ie MM10) for four shallow earthquakes of M_w 7.2 -8.2.

We seek to develop models for MM intensity that can be used given a coarse knowledge of the location, size and orientation of the larger faults, and sometimes the location of asperities. Earthquake rupture is a complex process, which includes important second-order features such as directivity effects, variable rupture velocities, and different frequencies of shaking emanating from different parts of the source. Modelling of that complexity is usually only possible by carrying out a detailed analysis of the seismic waveforms after an event occurs, and is not attempted here. Nevertheless, the moment release is distributed in some way over the whole fault surface, and therefore the models should include the first-order effect of moment contributions from all parts of the fault on the intensity of shaking at nearby locations.

With these considerations in mind, we have developed a new method of modelling spatial distribution of MM intensity using an empirical approach and a 2-D fault rupture model which allows for the presence of asperities. The intensity at any chosen point on the surrounding ground surface is then estimated by combining the contributions from all the elements of the source, in a way that respects both the logarithmic relationship between moment magnitude and seismic moment and a limiting point source model for intensity as a function of magnitude and distance from the source.

Our approach differs conceptually from that of Smith (1995), who presented a model for predicting near-source intensities based on an assumed relation between energy and MM intensity. Our method makes no assumption about the relation of MM intensity to any physical quantities beyond what is implied by our point-source model.

[1] *Tauranga, New Zealand (Life Member)*
[2] *GNS Science, Lower Hutt, New Zealand (Member)*

Our modelling method is discussed below, followed by comparisons of the modelled spatial distributions of intensity with the actual isoseismals of a selection of New Zealand earthquakes.

2 EARTHQUAKE DATA

The model was developed and optimised using source data and isoseismal geometry data for 44 New Zealand crustal earthquakes outside of the Taupo Volcanic Region, with magnitudes in the range M_w 5.0-8.2. The source data (given in Table 1) include the centroid depth h_c, depth to top of fault rupture h_t, magnitude M_w, and fault dip β (from D&R, 2005) with some revisions), and fault rupture length L, width W and average displacement D (from D&R, 2004). The latter three dimensions are derived assuming that the modulus of elasticity of the crust is 3×10^{10} N/m^2. The dimensions of the isoseismals of these events as used in this study (Table 2) were taken from D&R (2005), with some revisions. The uncertainties on the magnitudes come from D&R (2005), where we divided the magnitudes into four classes of quality, A, B, C and D, with standard errors of about 0.1, 0.15, 0.3 and 0.3 respectively. Of the standard errors of the estimates of h_c given in Table 2, 25 were formally assessed for events of M_w > 6.30 from 1922 onwards and for M_w > 5.40 from 1974 onwards (Anderson *et al*. (1993), Doser and Webb (2003), Doser *et al.* (1999), and Webb and Anderson (1994)). For the remaining 19 events the standards errors of the estimates of h_c were assessed informally taking account of the value of h_t and the width and dip of the rupture. The standard errors concerned are shown in italics.

As h_c is not used in our modelling analysis, the standard errors on the estimates of h_c are not used directly in the analysis of the standard errors discussed later, but they helped in assigning standard errors to our (informal) estimates of h_t, which are now discussed. First, as seen in Table 2, in the six cases where surface rupture was observed, h_t = 0 and the standard error is 0 also. Second, in 31 cases the standard error for h_t was taken as equal to that for h_c. In the remaining seven cases the depths of the tops the ruptures were considered to be well enough constrained to be assigned a lower standard error than that formally assigned to h_c for the corresponding event.

3 METHOD OF MODELLING THE SPATIAL DISTRIBUTIONS OF MMI

The method of modelling spatial distribution of Modified Mercalli (MM) intensity developed in the present study builds on that of D&R (2005) with the introduction of a planar 2-D, or biplanar 3-D, earthquake source representing the fault rupture of chosen dip(s), including asperities, for each earthquake. A single rupture surface is modelled as rectangle of area $A = L \times W$ (Figure 1A) and dip β (upper part of Figure 1C)), divided into a grid of smaller rectangles, as shown on Figure 1(A). Each small rectangle is considered as an earthquake source with moment magnitude M_{wi} dependent on its area and the displacement (slip). The total number of smaller rectangles is $n_L \times n_W$, where n_L and n_W are the number of subdivisions of length and width, respectively.

The displacement depends on whether the rectangle is an asperity, or not. The sum of the moments on all of the small rectangles equals the total seismic moment of the earthquake being modelled. We assume that if a rectangle is on an asperity, the displacement takes a value D_a, and otherwise it takes the value D_b, and that D is the average displacement over the whole rupture surface. The distribution of asperities/slip on the rupture surface is not known for any New Zealand earthquakes. Therefore a parametric study has been carried out, with the distributions of areas of asperities and non-asperities and the respective displacements on them being derived from data from 10 Californian earthquakes (Table 3) presented by Somerville *et al.* (1999). These data are plotted graphically on Figure 2, in terms of the normalised asperity area $A_{ar} = A_a / A$, the normalised asperity displacement $D_{ar} = D_a / D$ and the normalised non-asperity displacement $D_{br} = D_b / D$. Somerville *et al.* assumed that the minimum value of D_a is 1.5 D. Summing the moments on the asperities and non-asperities on the rupture surface, it can be shown show that

$$A_{ar}D_{ar} + A_{br}D_{br} = 1 \qquad (1)$$

where the area of non-asperities A_b is given by

$$A_b = A - A_a \qquad (2)$$

The ratio D_a/D may be expected to vary from earthquake to earthquake. For present purposes we adopt a constant value of 1.83 for this ratio, which is a representative value from the earthquakes in California (in the middle of the cluster of data points on Figure 2).

Considering the Californian events in Table 3, it is found that the moment M_0 released per unit area from the asperities is greater than that from the non-asperities by factors ranging from 2.0 to 6.2. It is also found that the non-asperities nevertheless contribute c.50 – 70 percent of the total seismic moment released. In the next section we will examine the influence of different arrangements of asperities on the spatial distribution of MM intensity.

Considering the areas of the asperities assembled by Somerville *et al.* for 10 Californian earthquakes it is found that the average of the ratio A_a/A for these events was 0.21. We adopt this value generally as a constant for the earthquakes in this study, but recognising that in reality this ratio would vary from earthquake to earthquake, we have carried out a sensitivity test (using alternative values of 0.1 and 0.33) on one earthquake.

For any given earthquake, if A and D are known and A_{ar} and D_{ar} assigned, then A_{br} and D_{br} can be found from Equations 1 and 2, so M_{wi} can be determined for all the rectangles on the rupture surface. Having adopted $A_{ar} = 0.21$ and $D_{ar} = 1.83$, it then follows from Equation 1 that $D_{br} = 0.78$. The values of D_a and D_b for these assumed values of A_{ar} and D_{ar} are given for each of the New Zealand earthquakes in Table 1. The above values are used in all the cases studied below, except that of Figure 18. It is seen on Figure 2 that (excluding the Morgan Hill outlier) D_{ar} lies in the range 1.5-2.1 and D_{br} lies in the range 0.67-0.85.

Five different distributions of asperities are considered in this study, the main two being: (1) evenly spaced asperities along the fault rupture (Figure 3A), and (2) centrally located asperities, i.e. all asperities placed at the centre of the fault length (Figure 3B).

Table 1: Source parameters for the 44 New Zealand crustal earthquakes considered in this study.

Event no.	*Date*	h_t (km)	h_c (km)	M_w	*FM*	β	*L* (km)	*W* (km)	*D* (m)	D_a (m)	D_b (m)
1*	**1855 Jan 23**	**0(0)****	**19(3)****	**8.20C**	**S**	**80**	**145**	**17**	**12.1**	**22.1**	**9.43**
	(biplanar)					**19**		**25**	**12.1**	**22.1**	**9.43**
2	1888 Aug 31	0(0)	8(2)	7.10C	S	90	38.3	15.2	3.24	5.93	2.53
3*	**1901 Nov 15**	**4(4)**	**10(4)**	**6.78B**	**R**	**70**	**24.1**	**12.1**	**1.88**	**3.44**	**1.47**
4	1912 May 26	12(5)	15(*5*)	5.65B	N	45	4.3	4.3	0.61	1.12	0.48
5*	**1922 Dec 25**	**5(5)**	**10(5)**	**6.40B**	**S**	**70**	**13.9**	**9.2**	**1.15**	**2.10**	**0.90**
6	1926 Nov 11	3(2)	5(3)	4.60B	N	45	1.3	1.3	0.18	0.33	0.14
7*	**1929 Mar 9**	**0(0)**	**11(*4*)**	**6.95B**	**S**	**90**	**30**	**13**	**2.52**	**4.61**	**1.96**
8	1929 May 7	8(5)	10(5)	5.45B	S	90	3.4	3.4	0.48	0.88	0.37
9*	**1929 Jun 16**	**0(0)**	**9(*3*)**	**7.72B**	**R**	**46**	**64.3**	**21**	**10.4**	**19.0**	**8.11**
10*	**1931 Feb 2**	**1(+2)**	**15(*3*)**	**7.79B**	**R**	**55**	**90**	**28**	**7.11**	**13.0**	**5.54**
11	**1932 Sep 15**	**2(+3)**	**8(*3*)**	**6.79B**	**S**	**85**	**21.4**	**13**	**2.03**	**3.71**	**1.58**
12*	**1934 Mar 5**	**1(+1)**	**8(*2*)**	**7.36B**	**S**	**82**	**60**	**17**	**3.97**	**7.26**	**3.09**
13	**1942 Jun 24**	**4(1)**	**12(*6*)**	**7.07B**	**S**	**86**	**30**	**12**	**4.10**	**7.50**	**3.20**
14	1943 Aug 2	27(5)	31(*5*)	6.57B	S	53	17.7	10.4	1.76	3.22	1.37
15	1945 Sep 1	21(5)	28(*5*)	6.98B	S	82	32.2	13.9	2.82	5.16	2.20
16	1946 Jun 26	5(4)	9(*4*)	6.32B	S	89	12.3	8.7	1.32	2.42	1.03
17	1948 May 22	1(+2)	4(*4*)	6.36B	S	90	13.1	8.9	1.38	2.53	1.08
18*	**1951 Jan 10**	**7(4)**	**10(4)**	**5.93B**	**R**	**45**	**6.0**	**6.0**	**0.81**	**1.48**	**0.63**
19	1951 Jun 24	23(5)	25(5)	5.51B	S	NA	3.7	3.7	0.52	0.95	0.41
20	1953 Jul 4	3(2)	5(2)	5.28B	N	45	2.8	2.8	0.40	0.73	0.31
21	1957 Feb 22	13(4)	15(4)	5.25B	N	45	2.7	2.7	0.38	0.70	0.30
22	1959 May 22	40(2)	40(2)	5.29B	NA	30	2.9	2.9	0.40	0.73	0.31
23	1960 May 24	4(2)	9(*4*)	6.46B	N	67	15.1	9.6	1.55	2.84	1.21
24	1962 Jan 23	18(5)	20(5)	5.01B	N	45	2.1	2.1	0.29	0.53	0.23
25	1963 Apr 12	32(5)	35(5)	5.84B	S	90	5.2	5.2	0.74	1.35	0.58
26	1963 Dec 22	4(4)	6(4)	4.93B	N	45	1.9	1.9	0.27	0.49	0.21
27	1964 Mar 8	2(5)	5(+5)	5.89B	S	83	5.7	5.7	0.80	1.46	0.62
28	1966 Apr 23	13(5)	16(5)	5.75A	R	66	4.8	4.8	0.68	1.24	0.62
29*	**1968 May 23**	**0.5(+2)**	**10(*3*)**	**7.23A**	**R**	**45**	**30**	**20**	**4.31**	**7.89**	**3.36**
30	1968 Sep 25	0(0)	4(4)	6.27A	S	85	11.5	8.5	1.24	2.27	0.97
31	1971 Aug 13	6(2)	9(*2*)	5.70A	S	83	4.6	4.6	0.65	1.19	0.51
32	1972 Jan 8	5(3)	7(3)	5.26B	N	45	2.8	2.8	0.39	0.71	0.30
33	1974 Sep 20	23(5)	25(*5*)	5.55B	R	45	3.8	3.8	0.54	0.99	0.42
34	1974 Nov 5	14(3)	17(*3*)	5.44A	S	41	3.4	3.4	0.48	0.88	0.37
35	1975 Jun 10	36(2)	38(*2*)	5.62A	N	56	4.2	4.2	0.59	1.08	0.46
36	1976 May 4	5(4)	10(*4*)	6.51A	R	47	16.3	10	1.64	3.00	1.28
37	1976 Dec 5	1(+2)	3(+2)	5.10D	N	45	2.0	2.0	0.29	0.53	0.23
38	1979 Oct 12	5(6)	12(*6*)	7.23A	R	24	46.2	16.6	3.76	6.88	2.93
39	1984 Jun 24	9(3)	13(+*3*)	6.12A	S	83	9.2	7.5	1.05	1.92	0.82
40	**1987 Mar 2**	**0(0)**	**6(*1*)**	**6.53A**	**N**	**39**	**13.0**	**9.0**	**2.0**	**3.66**	**1.56**
41	1990 Feb 10	6(2)	9(*2*)	5.93A	S	90	6.0	6.0	0.84	1.54	0.65
42	1990 May 13	9(3)	13(*3*)	6.37A	R	40	13.3	9.0	1.40	2.56	1.09
43	1994 Jun 18	3(2)	6(*2*)	6.71A	R	47	21.7	11.5	2.07	3.79	1.61
44	1995 Nov 24	3(2)	6(*2*)	6.25A	S	46	11.2	8.3	1.22	2.23	0.95

Notes: FM = Focal mechanism. Events in bold type are those examined graphically in this study. Events with asterisk in left hand column are those plotted in this paper. * Events with an asterisk are discussed in the paper. ** The standard errors on the estimates for h_t and h_c are given in parentheses, and are discussed in the text.

Table 2: Isoseismal distance data used for crustal New Zealand earthquakes.

Event No.		MM3		MM4		MM5		MM6		MM7		MM8		MM9		MM10	
		a	*b*	*a*	*b*	*a*	*B*	*a*	*b*	*a*	*b*	*a*	*b*	*a*	*b*	*a*	*b*
1*	**1855 Jan 23**							**270**	**244**	**204**	**170**	**144**	**122**	**93**	**35**	**33**	**11**
2	1888 Aug 31						199		105	105	24	56	16	22	7.8		
3*	**1901 Nov 15**			**290**		**180**	**185**	**128**	**85**	**64**	**42**	**25**	**17**	**12**	**4**		
4	1912 May 26			192	108	99	60	28	26								
5*	**1922 Dec 25**			**300**		**190**	**168**	**92**	**70**	**54**	**32**	**28**	**16**				
6	1926 Nov 11			50	50					4	4						
7*	**1929 Mar 09**			**300**		**224**	**210**	**94**	**80**			**34**	**20**	**20**	**7**		
8	1929 May 07			213	176	116	98	60	38	26	19						
9*	**1929 Jun 16**					**431**		**281**	**210**	**185**	**134**	**98**	**68**	**50**	**21**	**32**	**9**
10*	**1931 Feb 02**			**449**		**315**		**216**		**149**	**77**	**101**	**45**	**49**	**22**	**34**	**8**
11	**1932 Sep 15**			**378**		**220**		**94**	**100**			**48**	**32**	**22**	**14**		
12*	**1934 Mar 05**			**360**		**220**	**263**	**111**	**123**	**75**	**65**	**62**	**27**	**35**	**14**		
13	**1942 Jun 24**			**412**		**256**	**250**	**136**	**165**	**74**	**80**	**45**	**34**				
14	1943 Aug 02			265	200	72	100										
15	1945 Sep 01			335													
16	1946 Jun 26	338		232		161				27							
17	1948 May 22			196	126	116	80							(2)			
18*	**1951 Jan 10**			**170**	**190**			**37**	**29**	**32**	**32**	**10**	**10**				
19	1951 Jun 24			241	135	131	71										
20	1953 Jul 04	158	158			32	32										
21	1957 Feb 22			116	83	71	37										
22	1959 May 22	181		124		75	87	20	20								
23	1960 May 24			288	288	125	108										
24	1962 Jan 23			179	138	58	53										
25	1963 Apr 12	208		131	125	67	54	35	29								
26	1963 Dec 22					33	25	19	14	12	7						
27	1964 Mar 08			248	225	193	131										
28	1966 Apr 23			200		113	95	50									
29*	**1968 May 23**			**530**		**340**		**162**	**112**	**112**	**64**	**40**	**34**	**23**	**15**	**10**	**7**
30	1968 Sep 25			300				142						(2)			
31	1971 Aug 13			237		135	118										
32	1972 Jan 08			115	95	69	44	19	19	6.8	6.8						
33	1974 Sep 20	316		187	137												
34	1974 Nov 05			240	255	120	76	50	30								
35	1975 Jun 10			213	168	71	50	25	21								
36	1976 May 04					144	115										
37	1976 Dec 05			69	65	51	46	38	29	19	14						
38	1979 Oct 12						237										
39	1984 Jun 24					163	114	63	45								
40	**1987 Mar 02**			**196**		**121**	**138**	**47**	**51**	**26**	**25**	**19**	**14**	**12**	**6**		
41	1990 Feb 10			194				50.8	29								
42	1990 May 13			233	228	109	119	53	46	32	33	15	16.1				
43	1994 Jun 28						100		62								
44	1995 Nov 24		150														

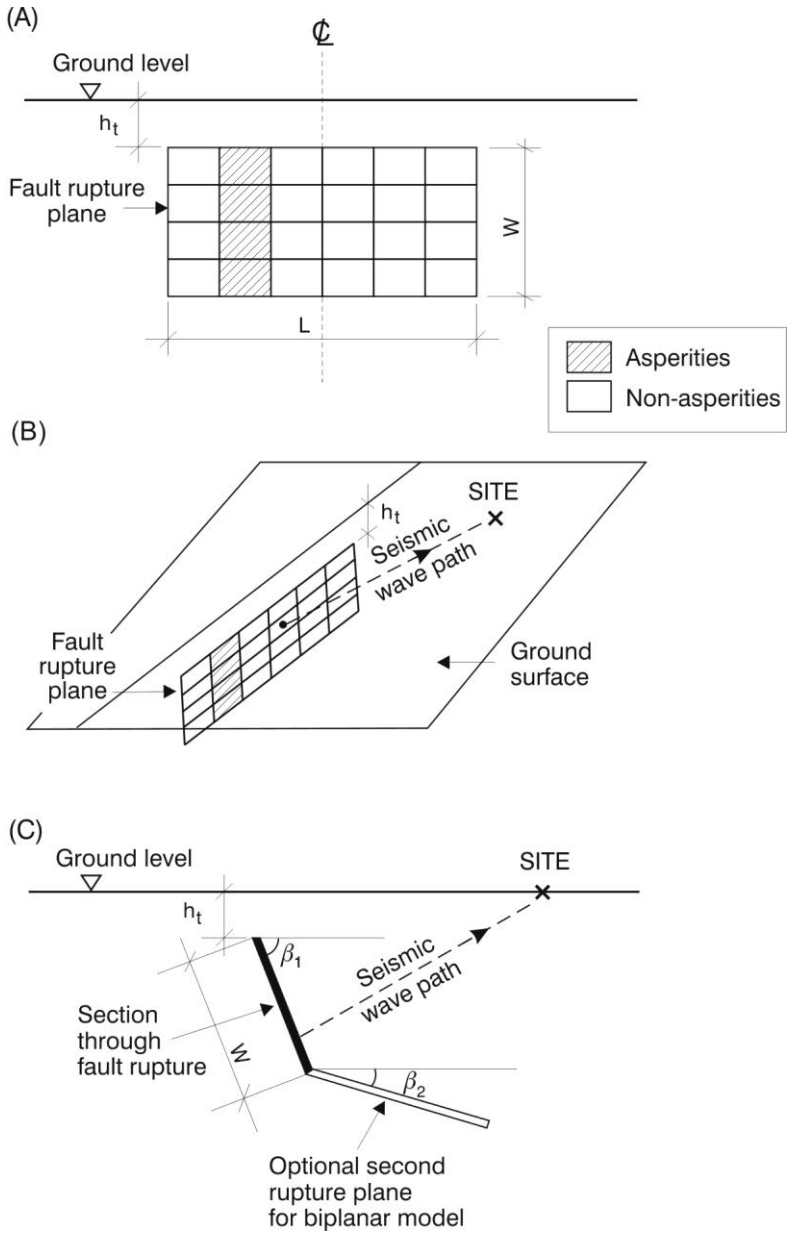

Figure 1: ***Simplified geometry of the fault rupture model with asperities as a 2-D or 3-D (biplanar) source, and its relationship to any chosen site on the ground surface. The biplanar source is only shown in (C). Asperities can be located in any cell.***

The intensity at any chosen site on the ground surface (Figure 1B) is estimated by calculating the intensity at that point caused by the moment on a given rectangle on the rupture surface, allowing for a point source attenuation model of a similar form to that of D&R (2005), i.e.:

$$I = A_1 + A_2 M_w + A_3 \log_{10} R + A_4 h_c \qquad (3)$$

Here, the "distance term" R is given by $R = (r^3 + d^3)^{1/3}$, where r is the median distance of the top of the source (or element of the source) from the site. In what follows, R is referred to simply as the "distance". No dependence of intensity on focal mechanism is considered in this model, and the distribution of residuals suggests that any such dependence is slight (see next section).

In order to allow for the geometry of the source in the estimation of intensity, we introduce the concept of effective distance, which can be applied when an earthquake is subdivided into a number of notional sub-events distributed over the source region. It is assumed that the intensity resulting from n sub-events of seismic moment M_0/n at distances $R_1, \ldots, R_n$ is the same as that from a single event of seismic moment M_0 at some distance, called the effective distance R_{eff}, which conforms to the relation

$$\frac{n}{R_{eff}{}^k} = \sum_{i=1}^{n} \frac{1}{R_i{}^k} . \qquad (4)$$

The combined intensity is obtained by applying the single-source model to the magnitude corresponding to a seismic moment M_0 at the effective distance R_{eff}.

The inverse power relation (Equation 4) is a mathematically convenient form, in which the value of the exponent k determines the different contributions to the effective distance from sub-events at different distances. It can be shown that the model proposed by Smith (1995) satisfies Equation 4, with $k \approx -0.6A_3$. The limiting values of k (0 and ∞) correspond to unrealistic extreme scenarios in which all sub-events contribute equally, regardless of their distance from the site, and when only the nearest sub-event contributes. Appendix 1 shows that, if the limiting point-source model is as in Equation 3, then k is determined by the fitted parameters A_2 and A_3 and is given by $k = -1.5A_3/A_2$.

Table 3: Asperity and non-asperity parameters of 10 Californian earthquakes adopted or derived from Somerville *et al.* (1999)

		Rupture Area	Av. Displ.	Mod. of Elas.	Asp. Area	No. of Asp	Norm. Asp. Area	Av. Asp. Displ.	Norm. Asp. Displ.	Norm. Non-Asp. Displ.
Earthquake	$\mathbf{M_w}$	A ($\mathbf{km^2}$)	D (m)	$\mu^* \times 10^{10}$ $\mathbf{N/m^2}$	A_a ($\mathbf{km^2}$)		A_{ar}	D_a (m)	D_{ar}	D_{br}
Landers 1992	7.22	1035	2.69	2.7	293	3	0.28	4.95	1.84	0.67
Loma Prieta 1989	6.95	720	1.66	2.5	152	2	0.21	2.90	1.74	0.80
Northridge 1994	6.66	378	0.74	3.9	75	5	0.20	1.54	2.07	0.73
San Fernando 1971	6.53	161	1.50	3.0	43	1	0.27	2.40	1.60	0.78
Imperial Valley 1979	6.43	360	0.69	4.5	90	1	0.25	1.27	1.85	0.72
Superstition Hills 3 1987	6.33	161	0.78	2.8	35	2	0.21	1.37	1.78	0.79
Morgan Hill 1984	6.18	299	0.17	4.1	42	6	0.14	0.58	3.40	0.61
North Palm Springs 1986	6.14	266	0.17	4.0	34	1	0.13	0.37	2.10	0.84
Whittier Narrows 1987	5.97	100	0.26	3.8	17	4	0.17	0.53	2.16	0.76
Coyote Lake 1979	5.66	25	0.76	5.3	8	1	0.32	1.15	1.51	0.76

Note: $^*\mu$ is derived from M_0/AD

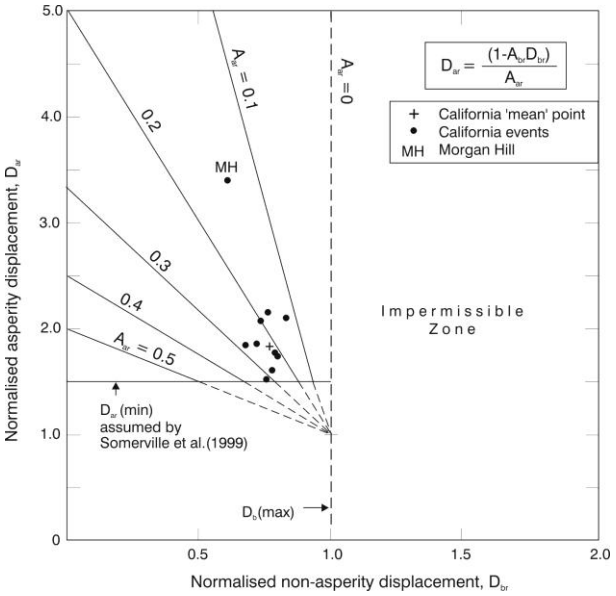

Figure 2: Relations between displacements and areas of asperities and non-asperities of fault ruptures for 10 Californian earthquakes, using data from Somerville et al. (1999).

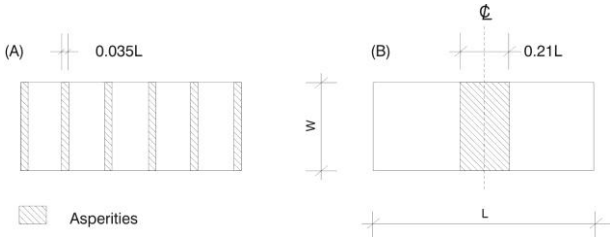

Figure 3: Distributions of asperities considered in most of the analyses where the area of asperities was 0.21 of the rupture area: (A) evenly spaced asperities, and (B) centrally located asperities.

A consequence of Equation 4 is that if all R_i are equal, say $R_i = R; i = 1, \cdots, n$, then $R_{eff} = R$. That is, the intensity resulting from a single event of seismic moment M_0 at distance R is the same as that resulting from n sub-events of seismic moment M_0/n at the same distance. This condition is necessary for the model to be self-consistent for sites in the far field, where the point-source model is a good approximation.

The effective distance (Equation 4) is only defined in relation to sub-events of equal size M_0/n. Note that this is no limitation in practice. If the source is divided into cells of equal area, as shown in Figure 1, then the moment, M_a of a notional sub-

event on an asperity is greater than that, M_b, on a non-asperity, with $M_a = \alpha M_b$, where $\alpha = D_a/D_b$. However, it is shown in Appendix 2 that a sub-event with moment M_a at distance R is equivalent to one of moment M_b at distance $R\alpha^{-1/k}$. Because of this trade-off between seismic moment and distance, the calculation of intensity at a remote point can always be reduced to combining the effects of notional sub-events with equal seismic moments.

As the source elements are reduced in size and the number n of notional sub-events consequently increased, the effective distance converges. For sufficiently small elements (large n), the effective distance is very close to the limiting value. For fitting of the models, the values $n_L = 27$ and $n_W = 9$ were used, giving $n = 243$ cells on each rectangular fault surface.

The parameters A_1, A_2, A_3, A_4 of the model were fitted by minimising the sum of squares of the intensity residuals at points on the isoseismals in the along-strike (a) and strike-normal (b) directions. Note that for $\beta \neq 90^o$, there is no symmetry in the b-direction distances and so it is necessary to consider two points on the isoseismal, one each side of the line of the top of the fault.

After some trial and error, the parameter d was fixed at 4 km. In the model of D&R (2005), where the optimal value of d ranges between 10 and 12 km, this parameter controls the maximum of the modelled intensity and prevents it from becoming infinite at the point source. In the present distributed-source model, it again prevents the modelled intensity from becoming infinite by moderating the contribution to the intensity at a point of interest from cells in the fault plane very close to it. When formally optimised, d is about 9 km, at which value the residual standard error is reduced insignificantly, but the model is then much closer to that of D&R (2005) and the benefit of distributing the source is partly negated. However with $d = 9$ km it was found that the near-source intensities of the largest earthquakes were unsatisfactorily underestimated, and $d = 4$ km gave a more satisfactory fit to the near-source intensities, without much increase in the residual standard deviation. When d is reduced below 4 km, the residual standard deviation becomes significantly larger. The chosen value is thus a compromise that fits the data well while preserving the intention of the present model to investigate the possible effects of source distribution and asperities on the near-source intensities.

The fitted parameter values for the terms in Equation 3 for the main two asperity distributions are as given in Table 4. Also given are their standard errors and the residual standard errors of each model. It can be seen that the parameter values are almost identical for evenly spaced and centrally located asperities, reflecting the relatively small number of observations close to large earthquake sources, and also indicating that for these near-source data the fitted values are rather similar under both distributions of asperities. This suggests that either set of parameter values may be used for modelling other geometric arrangements of asperities. For modelling with no asperities the parameter values for the evenly space asperities case are preferred.

It is noted that the regressions were carried out using a planar model of the 1855 earthquake (with dip = 80º and $W = 42$ km), rather than its biplanar model, which was developed late in the study.

Table 4: Attenuation model parameter estimates and standard errors (s.e.), and residual standard errors (RSE).

	Evenly spaced asperities*		Centrally located asperities	
Parameter	**Estimate**	**s.e.**	**Estimate**	**s.e**
A_1	4.78	0.23	4.78	0.23
A_2	1.12	0.04	1.12	0.04
A_3	-3.25	0.06	-3.24	0.06
A_4	-0.0082	0.0023	-0.0080	0.0023
d	4 km (fixed)		4 km (fixed)	
RSE	0.45		0.46	

Notes: *For the case of no asperities use these parameter values.

4 GOODNESS OF FIT

Figure 4 shows plots of residuals against fitted values, magnitude, fault length, along-strike and strike-normal isoseismal semi-diameters (a and b) respectively, and box-plots of the residuals by focal mechanism. In the plot of residuals against fitted values, the points lie on parallel lines with unit spacing because the original intensities to be fitted were all integers. The graph of residuals against fault width (not shown) was similar to that against fault length. From these plots we note that there is no obvious trend in the residuals with respect to magnitude, fault dimensions, or isoseismal distances, but that the residuals tend to be small at short isoseismal distances, indicating a relatively good fit to the near-source data. Also, the box-plot shows that the distribution of residuals is similar for strike-slip, normal, and reverse faults, although the larger residuals (those with absolute values close to or larger than one) are all associated with strike-slip faults.

The residual standard errors of our models (Table 4) are 0.45 and 0.46 for evenly spaced and centrally located asperities, respectively. These are slightly greater than the residual standard errors of the D&R (2005) models, which are 0.43 and 0.43 in the along-strike direction, and 0.43 and 0.45 in strike-normal direction for the "Focal-mechanism" and "Main-seismic-region" models, respectively. However, no store should be laid by these small differences, because the present data set contains about 30 fewer earthquakes than were used by D&R (2005), and the present models contain many fewer fitted parameters than the earlier ones. Also, in this study magnitudes have been regarded as fixed, rather than uncertain. The uncertain magnitude model used in D&R (2005) tends to reduce the residual standard error, by allowing the model to fit to an earthquake magnitude slightly different from the central

estimate. Taking all these matters into consideration, the present residual standard errors indicate a satisfactory fit to the data, comparable to that of D&R (2005), and a good fit to the near-source data. (The improved fit of our new models specifically to the MM10 and MM9 isoseismals of our largest earthquakes is evaluated below in our discussion of Figures 7 and 8 and Table 5.) It is also noted that the above residual standard errors are comparable to those obtained in strong motion modelling, such as those of McVerry *et al.* (2006).

Note that only a minor fraction of the residual variance can be explained by uncertainties in the earthquake source data. Applying approximate formulae for the standard errors of functions of random variables (Kendall and Stuart, 1977, p246), it is seen that magnitude uncertainties account for about 5%, 10%, 50% and 50% of the residual variance for magnitude classes A, B, C and D, respectively, and uncertainties in h_t and for less than 5%. Moreover, the standard errors of isoseismal radius determination, although not formally assessed, are considered to be no greater than about 5 km in most cases. It follows that in most cases this source of uncertainty accounts for less than 10% of the residual variance. Since only 3 of the 44 earthquakes are in classes C or D, the residual variance can therefore be mostly attributed to un-modelled complexities in the earthquake rupture process, as discussed in section 1.

In the absence of isoseismal data on large earthquakes with normal focal mechanisms the current model is only verified for use on strike-slip and reverse events.

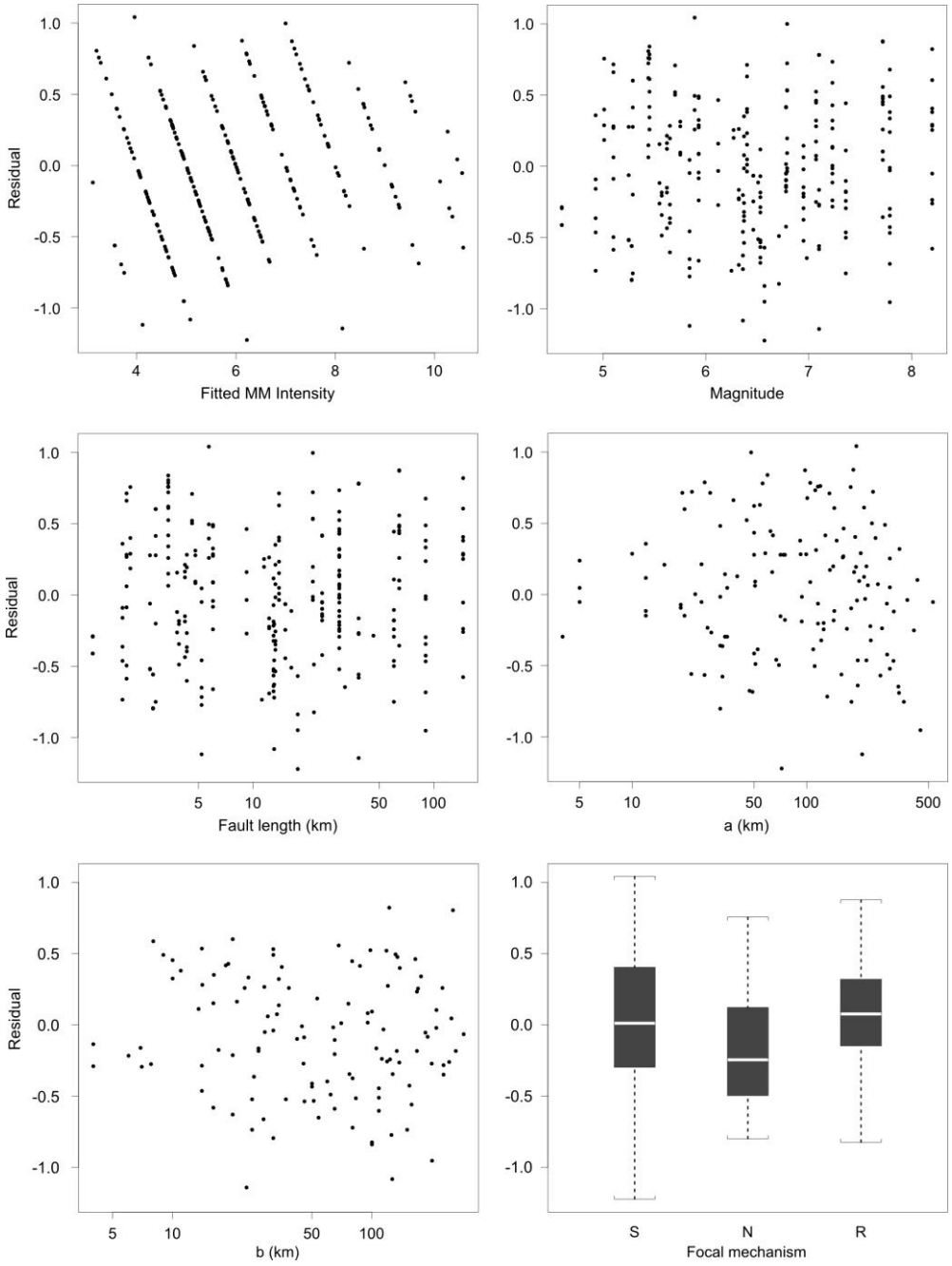

Figure 4: Plots of residuals considering fitted MM intensity, M_w, L, a, b, and focal mechanism.

Table 5: Results of a comparison between the fits of the 2-D and 3-D (biplanar) models with the D&R (2005) models to the data for MM10 and MM9 isoseismal half-lengths, *a*, and half-widths, *b*, for the six largest events in the data set as plotted on Figures 7 and 8.

Event **M_w** **Dip**		**1929/3** **6.95** **90º**	**1968** **7.23** **45º**	**1934** **7.36** **82º**	**1929/6** **7.72** **46º**	**1931** **7.79** **55º**	**1855** **8.2** **80º,19º**
	Isoseisl. direction						
MM10	*a*	NA	=	NA	2D	2D	P3D
	b	NA	2D	NA	2D	2D	05
MM9	*a*	2D	=	2D	2D	05	3D
	b	2D	2D	2D	2D	2D	05

Notes: 2D, 3D or 05 indicate the better fitting model. P3D see text. In the *b*-direction the mean of the up-dip and down-dip values is taken for the values of the 2-D and 3-D models for comparison with the single *b* values available from the D&R 2005 model.

Table 6: The residuals of the isoseismal sizes predicted by the 2-D and 3-D (biplanar) models with respect to the data for MM10 and MM9 isoseismal half-lengths, *a*, and half-widths, *b*, for the six largest events in the data set as plotted on Figures 7 and 8.

Event **M_w** **Dip**		**1929/3** **6.95** **90º**	**1968** **7.23** **45º**	**1934** **7.36** **82º**	**1929/6** **7.72** **46º**	**1931** **7.79** **55º**	**1855** **8.2** **80º,19º**
	Isoseisl. direction						
MM10	*a*	NA	0.1	NA	0.3	0.2	0.3
	b	NA	-0.1	NA	-0.1	-0.4	-0.3
MM9	*a*	0.1	0	0.3	-0.4	0.6	-0.3
	b	0.3	-0.1	-0.1	-0.1	-0.1	-0.3

Notes: In the *b*-direction the mean of the up-dip and down-dip values is taken for the values of the 2-D and 3-D models for comparison with the single *b* values available from the D&R 2005 model. The residuals are rounded to the nearest 0.1 unit of intensity.

5 DISCUSSION OF PREDICTED SPATIAL DISTRIBUTIONS

Introduction

As discussed above, the present model was optimised by fitting it to the isoseismal dimensions of 44 New Zealand earthquakes. For assessing our models, isoseismal maps and attenuation plots were made for 12 events chosen from those listed above in Table 1. Nine of those events were selected as sufficient for the following discussion.

Attenuation plots

The 2-D and 3-D source modelling shown on Figures 5, 7-9 is all done assuming that $A_{ar} = 0.21$ and that asperities are evenly spaced, as depicted on Figure 3A.

First consider the attenuation plots of the four smallest of those nine events, with magnitudes in the range 5.93-6.95, as shown on Figure 5. These events are the 1901 Cheviot, 1922 Motunau, 1929 March Arthur's Pass, and 1951 Cheviot earthquakes, respectively events numbered 3, 5, 7 and 18 in Table 1, where their source parameters are given. The attenuation plots are given for the *a*-direction (along-strike) and *b*-direction (strike-normal), and in the latter direction plots are given in both the up-dip and down-dip directions where the dip is non-vertical. Plots are shown for the new 2-D source model and the D&R (2005) model and the data points for the actual isoseismal dimensions. The focal mechanisms (FM), strike-slip and reverse, are indicated by S and R respectively.

On Figure 5 it is seen that the two models are close to identical in the far field, and are also quite similar in the near field except for the largest event in the along-strike direction (Figure 5Aa). In that figure it is seen that the new model deviates from the 2005 model near the end of the fault rupture, and closely matches the MM9 data point (see discussion of Figures 7 and 8). Two features of the along-strike plots of the 2-D source model of the two largest events on this figure (Figures 5Aa and 5Ba) are the plateaus of the predicted intensity which terminate near the end of the fault rupture, and the *reverse curvature* in the attenuation line beyond that point This is an attenuation feature which we have not previously seen, and is explained later in this section.

Within the next part of our discussion we consider the modelling of New Zealand's largest historical earthquake, the M_w 8.2 Wairarapa earthquake of 1855. For this event we utilise the 3-D biplanar option of our model introduced on Figure 1 (C) in the specific form shown on Figure 6, using the preferred solution of Darby and Beanland (1992).

Now consider Figure 7, which show the attenuation plots of the four earthquakes in our data set which have MM10 isoseismals (Figure 14), and those of a further very large earthquake in which the intensity reached very close to MM10

(Figure 8). They comprise five of New Zealand's six largest historical crustal earthquakes, with magnitudes in the range 7.23- 8.2. These events are the 1855 Wairarapa, 1929 June Buller (Murchison), 1931 Hawke's Bay, 1934 Waione (Pahiatua) and 1968 Inangahua earthquakes, respectively numbered 1, 9, 10, 12 and 29 in Table 1, where their source parameters are given. The actual strike-normal isoseismal dimensions are plotted for both the up-dip and down-dip directions of the three reverse focal mechanism (FM) events.

The features of Figures 7 and 8 are similar to those discussed for Figure 5, but the divergence between the two models in the along-strike direction is seen to increase markedly with increasing magnitude and rupture length, and the reverse curvature in the attenuation line beyond the end of the rupture for the 2-D and 3-D source models is seen to be increasingly pronounced with increasing magnitude. The pronounced reverse curvature is seen to extend from near the end of the fault rupture out to about intensity MM7, i.e. over a distance of about 70 km. The reverse curvature is explained in the next sub-section.

By comparing Figure 5 with Figures 7 and 8, and particularly Figures 5Aa and 7Da, the threshold for substantial near-source effects in the along-strike direction is seen to be at about M_w 7 and L 25 km.

Considering the strike-normal plots of the three reverse faults (Figures 7Bb, Cb and Db), it is seen that the 2-D source model fits the data for the up-dip and down-dip directions well. This was possible because the tops of the fault ruptures were sufficiently accurately located in relation to the actual isoseismals.

Our primary interest is in modelling the isoseismals near-source intensities in large earthquakes, ie MM9 and MM10, as defined for New Zealand by Dowrick *et al*. (2008), and improving on what is possible with the model of Dowrick & Rhoades (2005). To examine the success of the 2-D and 3-D models we have measured which of (1) the 2005 model, or (2) the 2-D or 3-D model, is a better fit to each of the MM9 and MM10 data points of the five large earthquakes modelled on Figures 7 and 8. The results of this comparison are given on Table 5. Here it is found that of the 20 data points concerned, the better fit is provided by the 2-D or 3-D model in 14 cases, the 2005 model is better in 3 cases, they are equally good in 2 cases, and in one case the 3-D model is probably better (ie the MM10 a dimension for the 1855 earthquake (see discussion of Figure 14A)). It is thus clear that the 2-D and 3-D models are an improvement on the 2005 model for prediction of near-source intensities in such large shallow events.

In addition, again considering the MM9 and MM10 data on Figures 7 and 8, we have evaluated the residuals found from

$$I_{2,3D} - I_d$$

where $I_{2,3D}$ is the intensity predicted by the 2-D or 3-D model, and I_d is the data , ie intensity 9.0 or 10.0.

The residuals for the 20 data points concerned are listed in Table 6. The mean value of these residuals is -0.005 units of intensity, showing that the new models fit the near-source data of the largest earthquakes very well.

Returning to Figure 7Aa, the bumps on the plot of the 3-D source model over the length of the fault rupture are caused by the evenly spaced asperities on the rupture surface. The asperities model over the full area (simplified to 2-D form) of the rupture surface is shown to linear scale on Figure 9, as are the attenuation plot using the 2-D source model and the dimensions of the actual MM8, MM9 and MM10 isoseismals (assumed to be symmetrical about the mid-point of the fault rupture). The length of the actual MM10 isoseismal for this earthquake is discussed later, in relation to Figure14A. On Figure 9 the effect of the asperities is seen to be small, increasing the intensity locally by c. 0.15 intensity units. This is consistent with the fact that the top 10 km of each asperity releases only 1.5% of the total seismic moment. It was also found that the parts of these asperities located deeper than 5 km below the surface have negligible effect on the local increase in intensity (See also the discussion of the deepness of the asperities on Figure 18).

We now examine the effect of a different distribution of asperities from the evenly spaced ones of Figures 5, 7-9, i.e. we place all the asperities at the centre of the fault rupture (as on Figure 3B), considering the second and third largest earthquakes, the 1929 Buller and 1931 Hawke's Bay reverse faulting events. Their attenuation plots are shown on Figures 12A and 12B respectively. The difference in intensity at the centre of the fault rupture as given by these two distributions of asperities is more easily seen on Figure 13, where the two asperity cases for the Hawke's Bay earthquake (ie Figures 7B and 12A) are shown on the same plot. It is seen here that the central intensity is 0.2 intensity units greater in the centrally located asperities case than in the evenly spaced case where no asperity is placed.

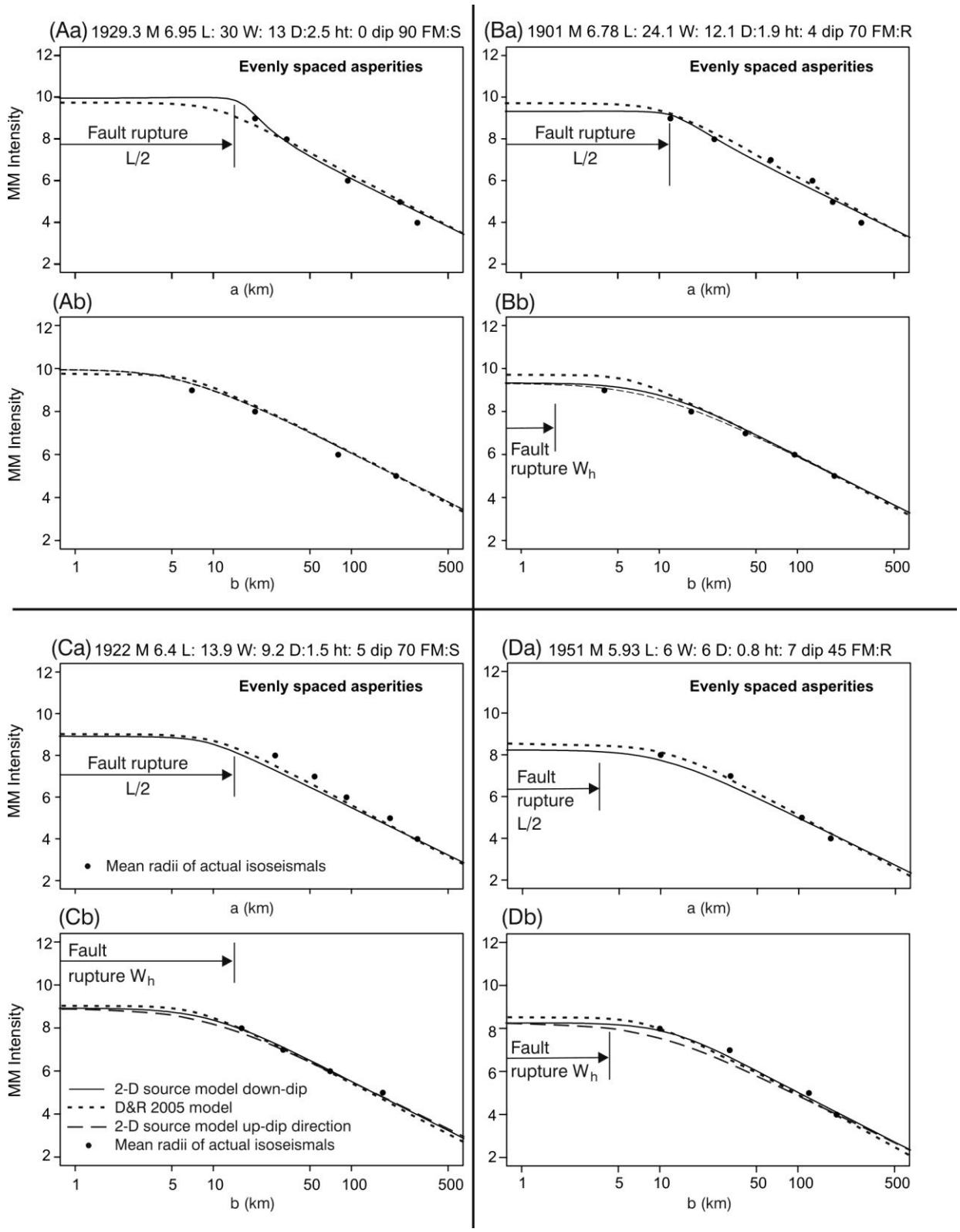

Figure 5: ***Attenuation plots of the 2-D source model and the D&R 2005 model against distance a and b data for four historical NZ earthquakes of M_w 5.93 – 6.95, L 6 – 30 km, and dip 45° - 90°. For non-vertical faults the strike-normal attenuation plots are given in both the up-dip and down-dip directions. The asperities are evenly spaced along the fault. W_h is the horizontal component of the rupture width. (Legend shown on Figure 5C. D&R 2005 is Dowrick & Rhoades (2005)).***

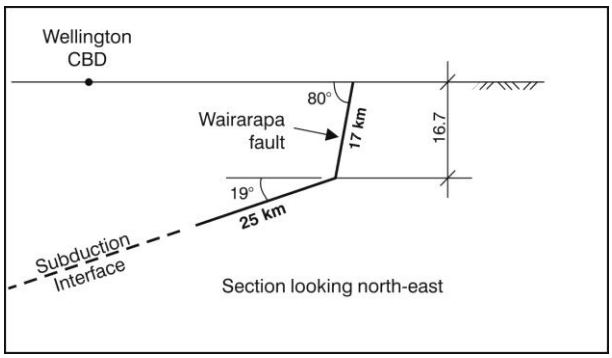

Figure 6: Cross-section through the source of the M_w 8.2 1855 Wairarapa earthquake, modelled as a biplanar fault rupture, following Darby and Beanland (1992).

Seismic source intensity

To explain the reverse curvature in the attenuation curves for the along-strike direction of the large earthquakes modelled on Figures 5A, 7, and 8, we consider the intensity of the energy release in these events. First we define *seismic source intensity*, I_s, as the moment released per unit area on a fault rupture surface during an earthquake, ie

$$I_s = \frac{M_0}{A} \qquad (5)$$

$$= \frac{\mu A D}{A}$$

Thus $$I_s = \mu_r D \qquad (6)$$

where μ_r is the regional crustal modulus of elasticity.

Normalizing Equation 6 with respect to $\mu_0 = 3 \times 10^{10}$ Nm

$$I_{s\mu_0} = \frac{\mu_r}{\mu_0} D \qquad (7)$$

For New Zealand, $\mu_r = \mu_0$, so for New Zealand the source intensity from Equation 7 becomes simply

$$I_{s\mu_0} = D \qquad (8)$$

On Figures 5A, 7 and 8 it is seen that *reverse curvature in the along-strike attenuation curves* occurs for near-surface New Zealand earthquakes with source intensities (ie D) of 1.9 (Figure 5Ba) to 12.1 (Figure 7Aa).

Now consider a large surface rupturing event similar to the 1934 Waione earthquake on Figure 8, ie with M_w 7.36, but (for simplicity) with dip = 90º and with no asperities. We compare the attenuation patterns for this moment release from two sources of very different intensity: (1) 60 km × 17 km = 1020 km^2, D = 4, and (2) 7 km × 7 km = 49 km^2, D = 83. Case (1) has the same source intensity as the earthquake of Figure 8, while case (2) is a hypothetical model of the same energy release with 21 times greater source intensity to the simulate something close to a point source. The attenuation curves for these two cases are plotted for comparison on Figure 10. The attenuation curves for the two cases have to be identical in the far-field, and the curves are seen to merge 80 km and 40 km from the centre of the rupture for the *a*- and *b*-directions respectively. The isoseismals from the two sources become essentially circular from intensity MM7 outwards. This is what happens with the actual isoseismals of the 1934 M_w 7.36 Waione earthquake as plotted on Figure 11, and as shown by the data points on Figure 10. On Figure 11(B) it is also seen that the near-point-source model of case (1) produces a virtually circular MM10 isoseismal.

Returning to Figure 10A, it is seen that the along-strike attenuation curve closely matches the actual length of the innermost (MM9) isoseismal (as noted above in relation to Figure 8A). For the long ruptures of Figures 7, 8 and 10, the intensity plateau must extend the full length of the fault trace, and the attenuation curve must also coincide with that of the point source in the far field, necessitating the reverse curvature seen on these along-strike attenuation plots.

Spatial distribution plots

Next we consider the spatial distribution of near-source ground shaking intensity for the four large events producing intensity MM10, i.e. the representation in plan of the attenuation plots of Figure 7 predicted by the 2-D source model, compared with the actual inner isoseismals, MM8 - MM10. These spatial plots are mapped on Figure 14, which also shows other map features such as coastlines, some roads, and some key place names. The focal mechanism (FM) of the first event is strike-slip (S) while the others are reverse (R).

First consider the M_w 8.2 1855 Wairarapa earthquake shown on Figure 14A. It is important to realise that due to the small population in this region in 1855, the actual isoseismals are not strongly constrained by data. Indeed the actual MM10 isoseismal surrounds a zone of unpopulated mountains and sparsely populated flat country where the intensity was defined entirely by environmental effects, landslides in the mountains and sand boils or lateral spreading on the (south-eastern) wet portion of the plains (Hancox *et al.*, 1997). As seen on the map, it was not possible to plot intensities around the south-western 30 km of the fault rupture because this zone is offshore, while the north-eastern 40 km or so of the fault rupture is not so close to the mountains as is the central portion (see the portion denoted "terrain less susceptible to landslides" on Figure 14A). There is a strong likelihood that if the whole length of the fault rupture had been in mountains, then the MM10 isoseismal would have been defined by landslides and seen to extend the whole length of the rupture, as is the case for the 1929 Buller earthquake (Figure 14C). (See also comments on the modelling of this very wide fault in the two paragraphs of discussion of Figure 21.)

Next consider the M_w 7.79 1931 Hawke's Bay earthquake shown on Figure 14B. Here the along-strike extent of the MM9 isoseismal is well defined by the robust MM8 intensities assigned outside the two ends of the MM9 isoseismal at Wairoa and Poukawa (see map), and MM9s inside it (not shown). The MM10 isoseismal has been drawn at its south-west end to enclose the very robust MM10 at Hastings, and could well have been found to extend further south-west (if suitable buildings had existed there). The location of the north-east end of the MM10 isoseismal lacks controls near the fault which is offshore in this zone. Constraint is provided by the MM9 assigned for Mohaka. As all the buildings in and near Mohaka were of timber, it was not possible to find indicators of MM10, such as were provided in abundance by brick buildings in and around Napier and Hastings. The asymmetry of both the modelled and actual isoseismals due to the westward fault dip of 55° is seen here in plan view, as well as on the attenuation plots of Figure 7Bb. For further discussion of the modelling of this earthquake, see particularly Figure 18.

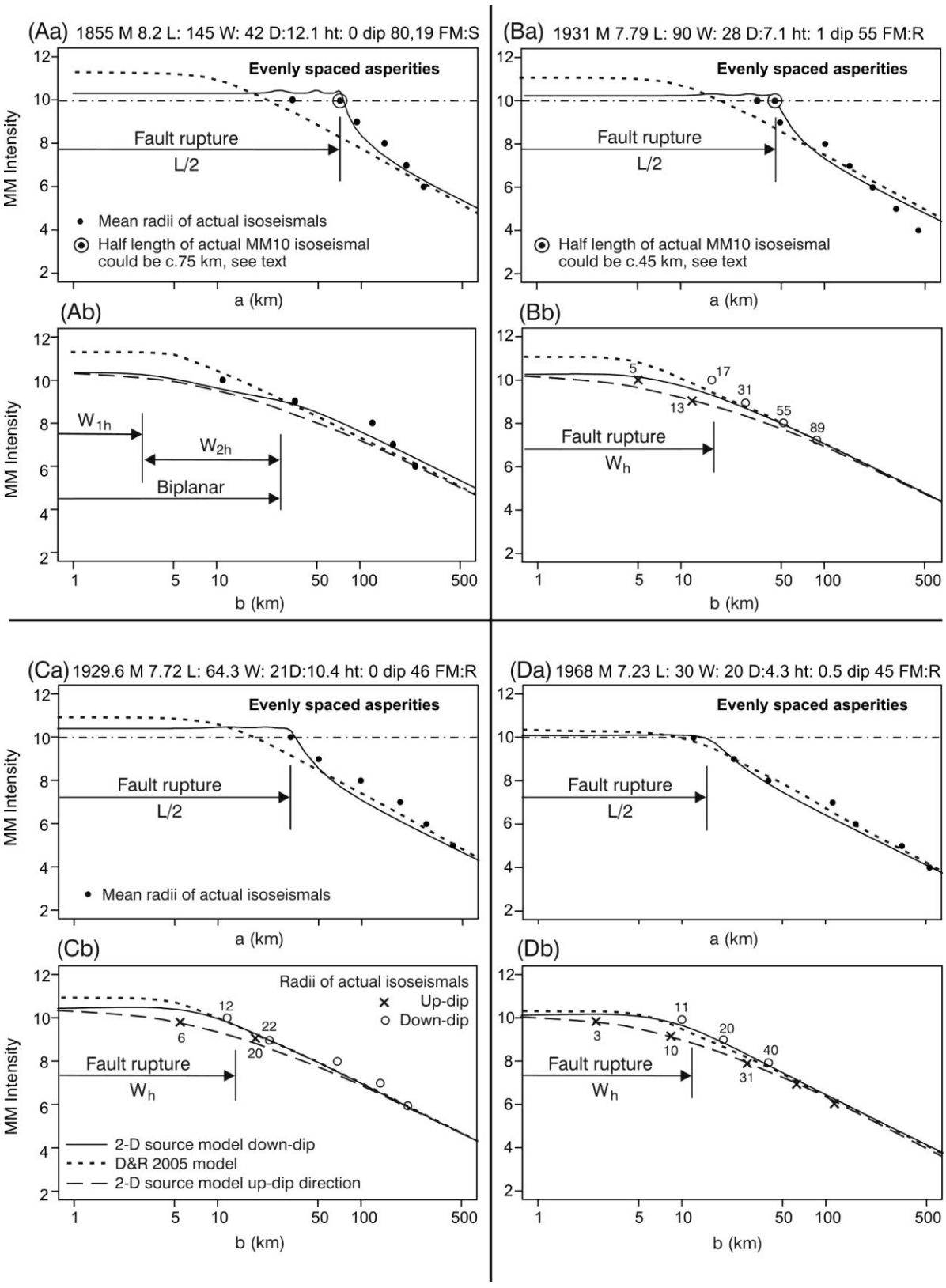

Figure 7: ***Attenuation plots of the 2-D and 3-D source models and D&R 2005 model against distance a and b data for four very large historical NZ earthquakes having MM10 isoseismals, with M_w 7.23 – 8.2, L 30 – 145 km, and dip 45° - 80°. The source for the M_w 8.2 earthquake is biplanar, see Figure 6. For non-vertical faults the strike-normal attenuation plots are given in both the up-dip and down-dip directions. Reverse and Strike-slip focal mechanisms are denoted FM:R and FM:S. The asperities are evenly spaced along the fault. W_h is the horizontal component of the rupture width (Legend shown on Figure 5C. D&R 2005 is Dowrick & Rhoades (2005)).***

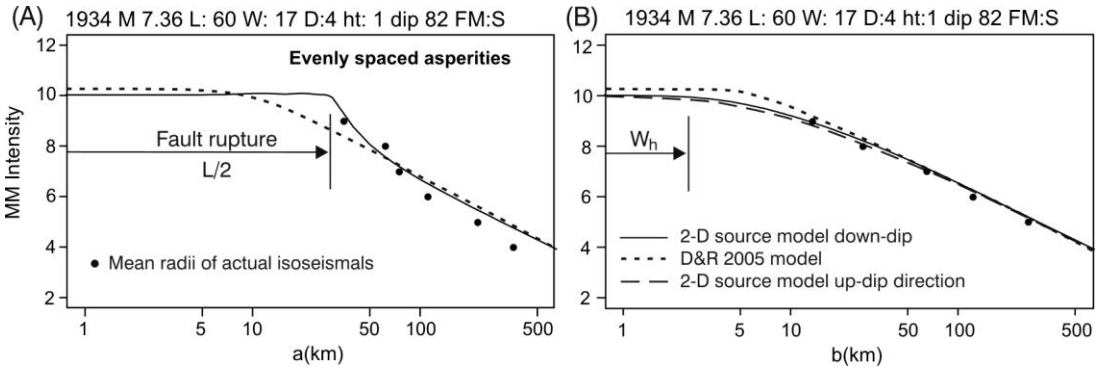

Figure 8: ***Attenuation plots of the 2-D source model and the D&R 2005 model against distance a and b for the M_w 7.36 1934 Waione (previously Pahiatua) earthquake. The asperities are evenly spaced along the fault (Legend shown on Figure 5C. D&R 2005 is Dowrick & Rhoades (2005)).***

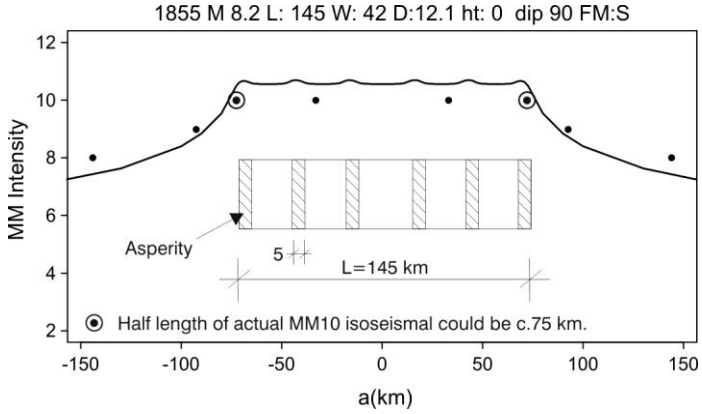

Figure 9: ***Plot of intensity along the top of the fault rupture for the M_w 8.2 1855 Wairarapa earthquake, as derived in Figure 7(Aa) but plotted to a linear scale, showing the effects of the asperities.***

It is noted that the isoseismal map of Dowrick (1998) for this earthquake has been revised (modestly) for the revised Atlas of Isoseismal Maps of New Zealand Earthquakes (Downes and Dowrick, in prep.).

Next consider the M_w 7.72 1929 Buller earthquake shown on Figure 14C. Unlike for the two previous earthquakes (Figures 14A and 14B), there are no offshore zones in the near-source region, but the MM10 zone was uninhabited, with no buildings as indicators of intensity. However the lack of population was due to the terrain being continuous and heavily-forested mountains, which suffered many landslides. The landslides helped to define the MM9 zone (Dowrick, 1994), and were the sole determinants of the MM10 zone (Hancox *et al* (1997) and Downes and Dowrick (in prep). In both the *a*- and *b*-directions, the sizes of the modelled and actual isoseismals are seen to be quite similar. The asymmetry of the modelled MM9 and MM10 isoseismals and the actual MM10 isoseismal, due to the eastward fault dip of 46°, are seen here in the plan view, as well as shown in the attenuation plots (Figure 7Cb).

Finally the plan view of our fourth MM10 earthquake, the 1968 M_w 7.23 1968 Inangahua earthquake is considered (Figure 14D). For this earthquake the near-source local intensities are all assigned from damage to buildings. The traditional felt reports have been supplemented by damage ratio data from Dowrick *et al.* (2001) in a study which used data from most privately-owned houses. The actual isoseismals used here are from a revision of the original 1968 map, which was created by Dowrick for the Atlas of Isoseismal Maps of New Zealand Earthquakes prepared by Downes and Dowrick (in prep). On Figure 14D, the along-strike location of the actual MM10 isoseismal in the south-west direction is constrained between the robust MM10 at Inangahua Landing and the robust MM9 at Rotokohu, while its extent in the north-east direction is limited by the robust MM9s at Lyell and nearby New Creek. This makes this isoseismal asymmetrical with respect to the length of the fault rupture, which is not the case for the modelled MM10 isoseismal. This point is discussed below in relation to Figure 16. The extent of the actual MM9 isoseismal is limited by the MM8s assigned in two locations near its perimeter, i.e. at Denniston in the north-west, and in the south around Reefton and nearby Waitahu. The strong asymmetry of the actual and modelled MM9 and MM10 isoseismals about the top of the rupture is caused by the fault dip of 45°, as also seen above on Figure 7Db.

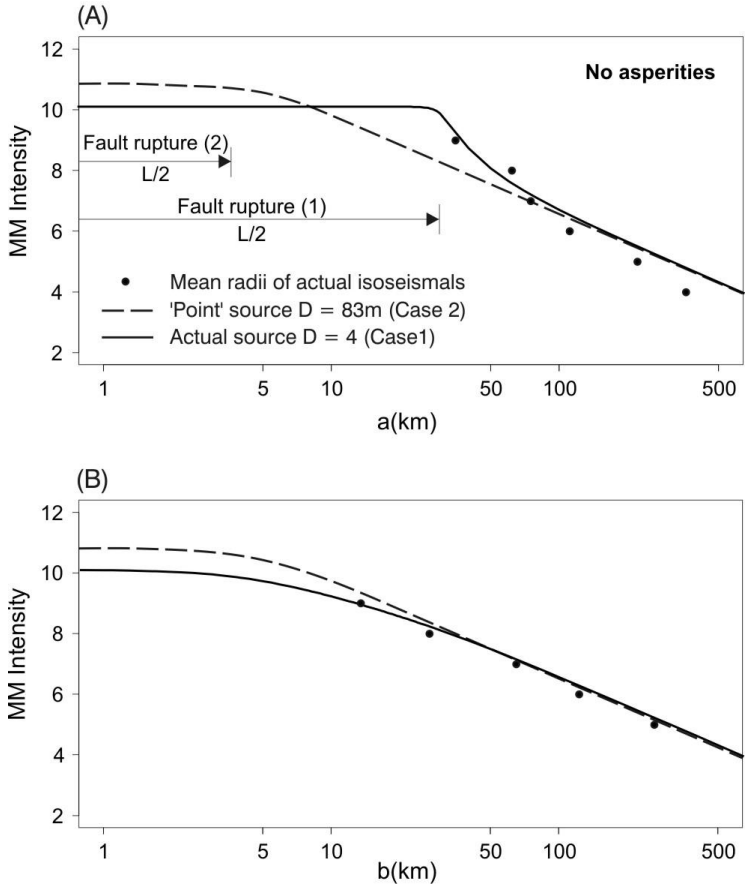

Figure 10: ***Attenuation plots of the 2-D source model against distance a and b for two source intensities, for earthquakes of M_w 7.36, h_t = 1 km, dip = 90° and no asperities, for Case 1: L = 60 km, W = 17 km, and D = $I_{s\mu_0}$ = 4, and Case 2 ("point" source): L = W = 7 km, and D = $I_{s\mu_0}$ = 83.***

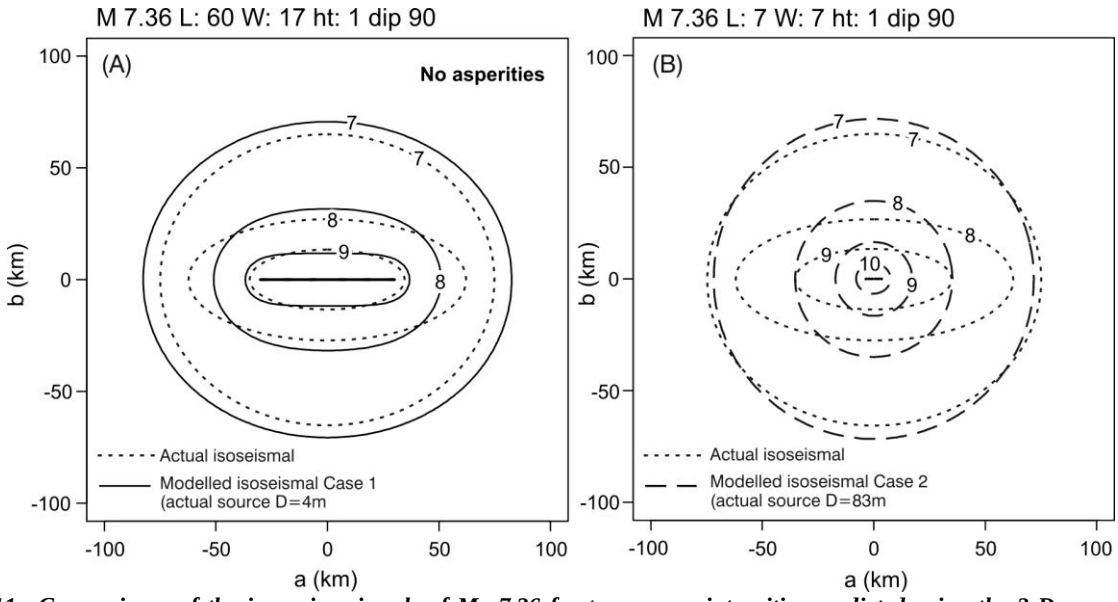

Figure 11: ***Comparisons of the inner isoseismals of M_w 7.36 for two source intensities predicted using the 2-D source model. Also shown are the actual isoseismals of the 1934 Waione earthquake. (A) Case 1: Actual source L = 60 km, W = 17 km, and D = $I_{s\mu_0}$ = 4, and (B) Case 2 "Point" source L = W = 7 km, and D = $I_{s\mu_0}$ = 83. (The corresponding attenuation plots are shown on Figures 10 and 8 respectively).***

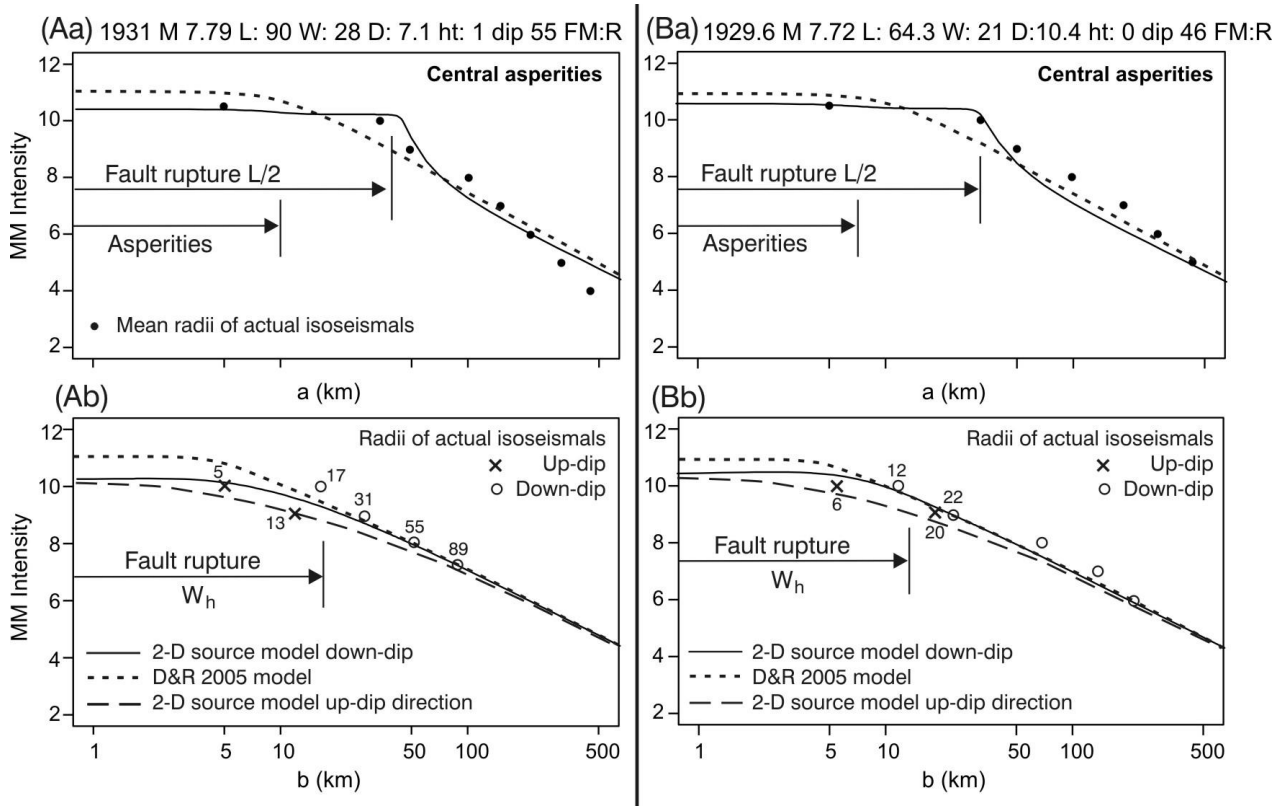

Figure 12: ***Attenuation plots of the 2-D source model the and D&R 2005 model against distance a data for (A) the 1931 Hawke's Bay and (B) the 1929 Buller earthquakes, of M_w 7.79 and 7.72, L 90 and 64 km, and dip 55° and 46° respectively. The asperities are centrally located on the fault, for comparison with the effects of evenly spaced asperities for these events on Figure 6. W_h is the horizontal component of the rupture width (Legend shown on Figure 8A. D&R 2005 is Dowrick & Rhoades (2005)).***

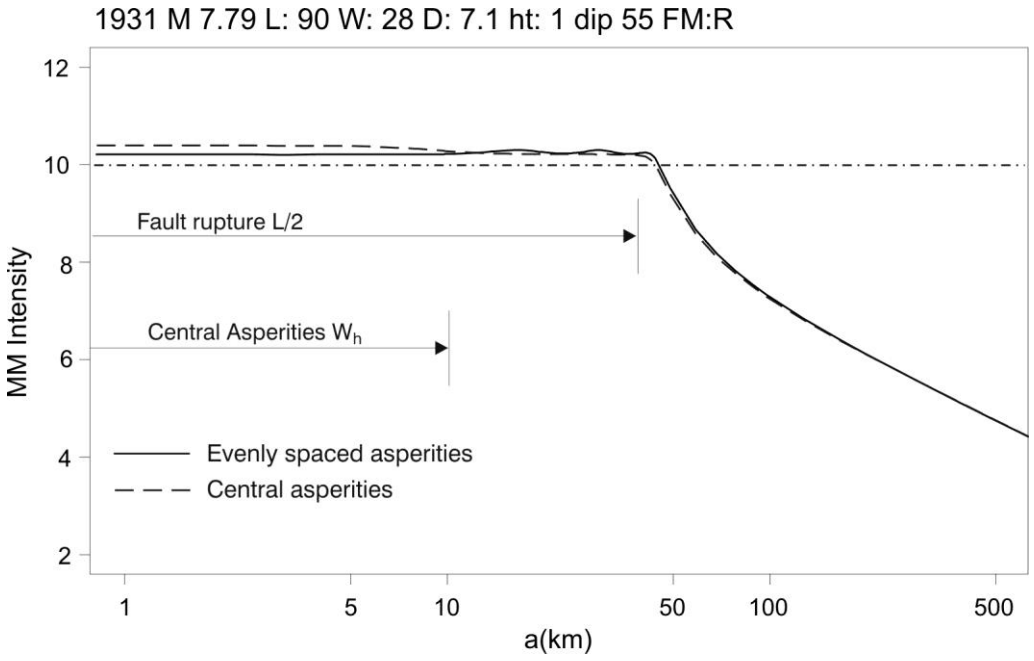

Figure 13: ***Attenuation plots of the 2-D source model for the 1931 Hawke's Bay earthquake, comparing the intensities caused by the evenly space asperities (from Figure 7B) with those caused by centrally located asperities (from Figure 12).***

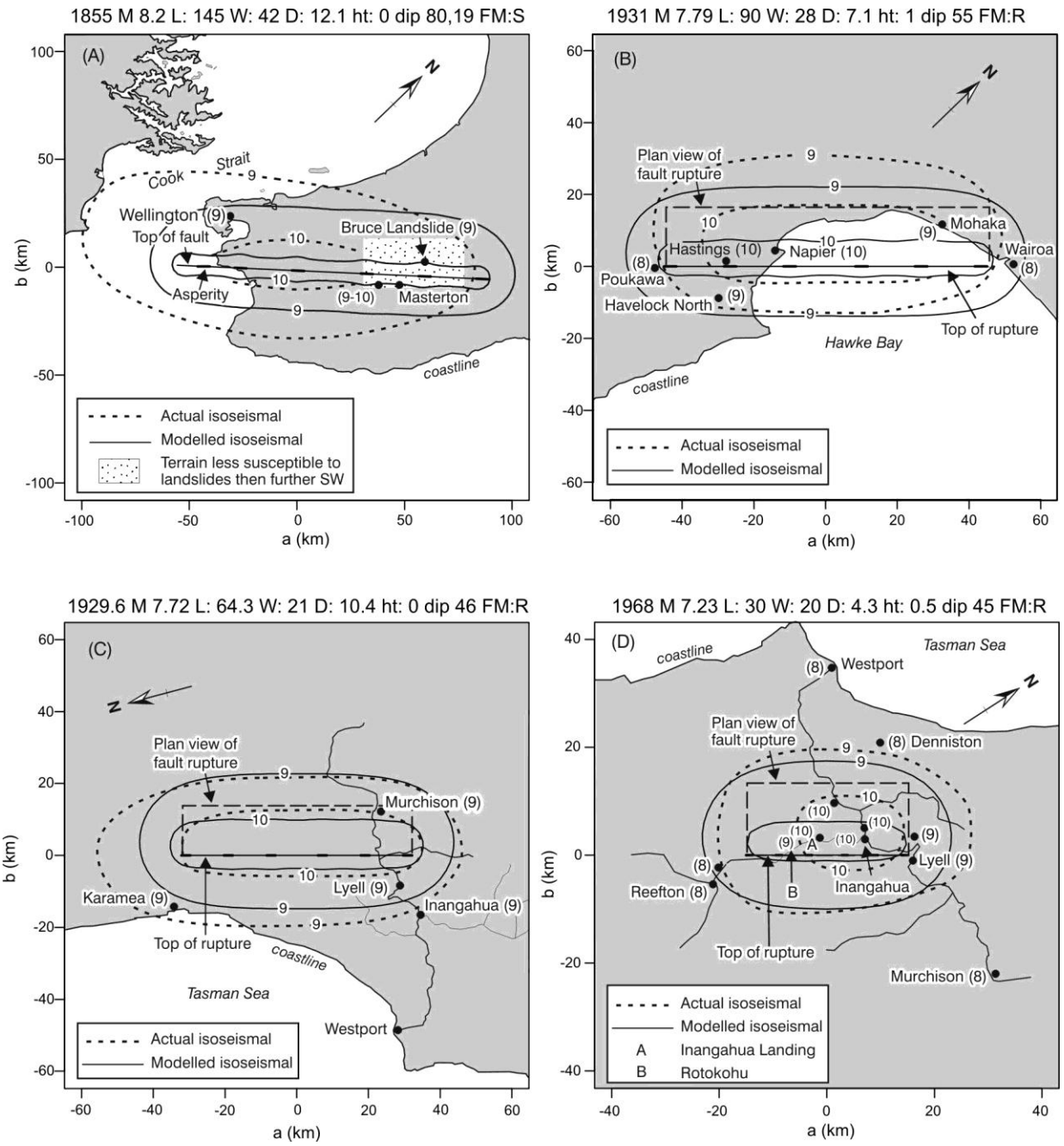

Figure 14: ***Comparisons of the MM9 and MM10 isoseismals from the 2-D source model (evenly spaced asperities, A_{ar} = 0.21) vs. actual, for (A) the M_w 8.2 1855 Wairarapa, (B) the M_w 7.79 1931 Hawke's Bay, (C) the M_w 7.72 1929 Buller and (D) the M_w 7.23 1968 Inangahua earthquakes. The top of the fault rupture is shown on the x-axis. As well as giving the isoseismal intensities in Arabic numerals, local intensities are given in brackets after some of the place names.***

Influence of lower displacements on parts of the rupture surface

Next the 1931 Hawke's Bay earthquake fault rupture is modelled with all its asperities located centrally and the non-asperities are divided into two levels of displacement with D_{br} reduced to 0.5 in zones at the ends of the rupture (Figure 15A). As seen on Figures 15B and 15C, this results in higher intensities near the centre of the fault and lower intensities at the ends of the rupture. Unlike in Figure 14B, the MM10 isoseismal no longer encloses the ends of the rupture, so there is a slightly better match with the length of the actual MM10 isoseismal. A much better match would be obtained if the modelled length of the rupture was shorter, say if L was taken as 80 km, as was estimated by Haines and Darby (1987). The modest local increase in intensity (0.25 units) at the centre of the rupture is consistent with the small local increases of MMI seen at the more localized asperities on Figure 9.

Influence of asymmetry of displacement in the along-strike direction

We now return to the 1968 Inangahua earthquake with a different model for the asperities from that adopted for Figure 14D, i.e., as shown on Figure 16A. In a dislocation study by Haines, discussed in Anderson *et al*. (1994), the slip was found to be uniform over the northern 20 km length of the rupture, tapering to zero over the southern 10 km (Figure 16A). This slip distribution was approximated to in the present study by the asperity and non-asperity distribution shown on Figure 16B. Using this asymmetrical 2-D source model, the predicted MM10 and MM9 isoseismals were as shown on

Figure 16C. Here it is seen that these isoseismals are asymmetrical in the along-strike direction, providing a better fit to the actual isoseismals than that shown on Figure 14D, found using evenly spaced asperities.

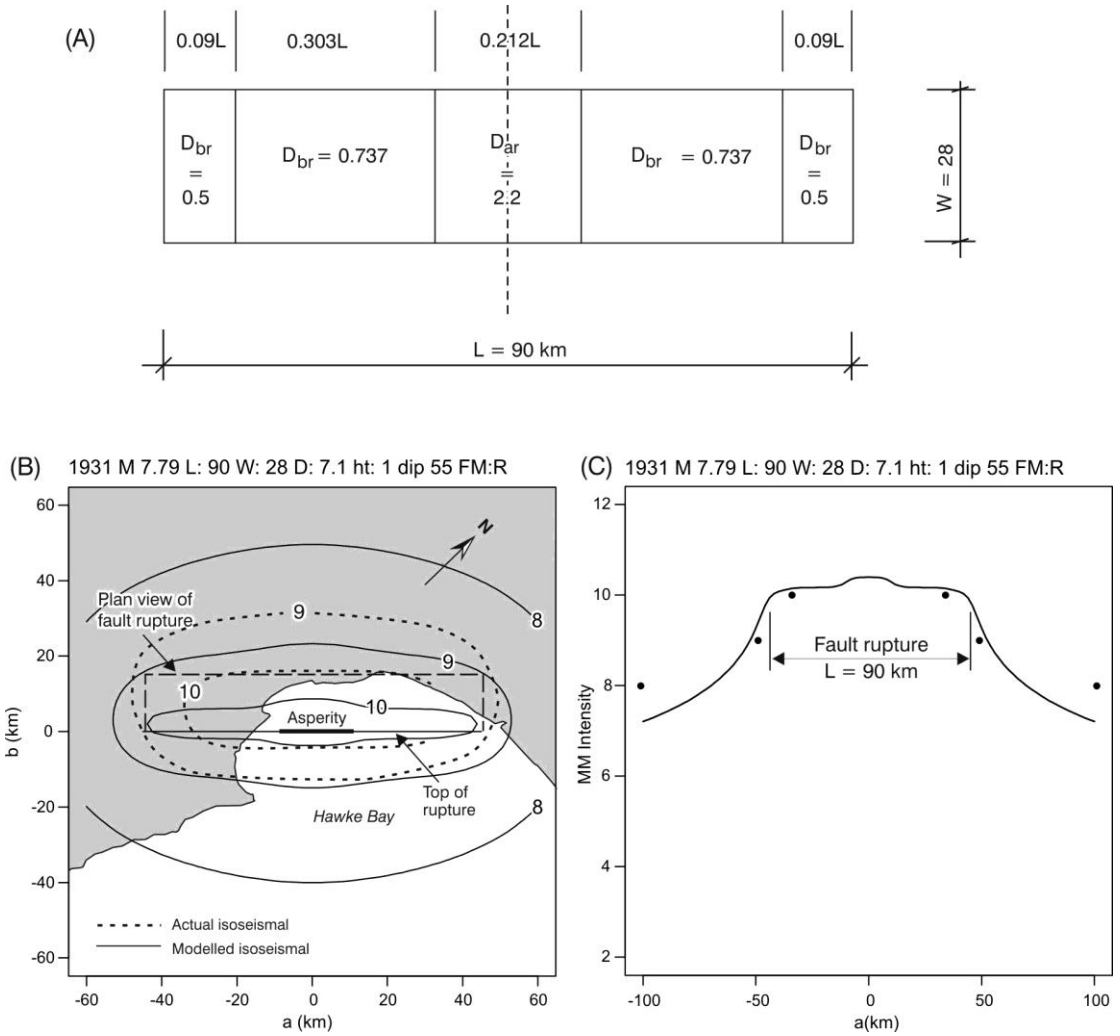

Figure 15: Comparisons of the MM9 and MM10 isoseismals from the 2-D source model (central asperities, A_{ar} = 0.21, with two levels of non-asperity displacements) vs. actual, for the M_w 7.79 1931 Hawke's Bay earthquake, (A) Asperity model, (B) Map of the actual MM9 and MM10 isoseismals and those modelled as shown on (A) above, and (C) Linear scale attenuation plot in the a-direction.

The along-strike co-ordinate of the centroid of the seismic moment released by this asymmetrical source is located at a = 2.1 km (Figure 16B), and as a consequence the common centroid of all of the predicted isoseismals is offset 2.2 km in the along-strike direction (ie. to the northeast on Figure 16C).

From Figures 13-17, and others not shown here, it has been found that predicted MM10 isoseismals may or may not enclose the top of the rupture, while MM9 isoseismals enclose the top of the rupture if $M_w \geq 7, L > 20$ and $h_t \leq$ c. 2 km. These findings are supported by the data.

Sensitivity to area of asperities

Next consider the sensitivity of the isoseismal pattern to variations in the proportion of the rupture surface that is comprised of asperities. For this purpose two different values of A_{ar} , i.e.. 0.1 and 0.3, were located centrally on the rupture of the 1931 Hawke's Bay earthquake. The resulting inner isoseismals are shown on Figures 17A and 17B. First considering the case of the smaller area of asperities, i.e. $A_{ar} = 0.1$, on Figure 17A it is seen that the inner isoseismals are only slightly affected by this small area of asperities, and they are very similar to those of the evenly spaced asperity case of Figure 14B. It follows that with a substantially larger proportion of asperities, where $A_{ar} = 0.3$, the shapes of the inner isoseismals are clearly more affected (Figure 17B).

The foregoing comparisons of Figures 14D vs. 16C, 14B vs. 15B and 17A vs. 17B can be summarized as follows: Patterns of distribution of displacement on the rupture surface are modestly influential on the size and shape of the MM10 isoseismal. For any given event, as the asperities commonly contribute about 30-50 percent of the seismic moment, the non-asperity area contributes 50-70 percent of the moment. This means that the non-asperity area is generally at least as influential as the asperities in dictating the size and shape of the isoseismals.

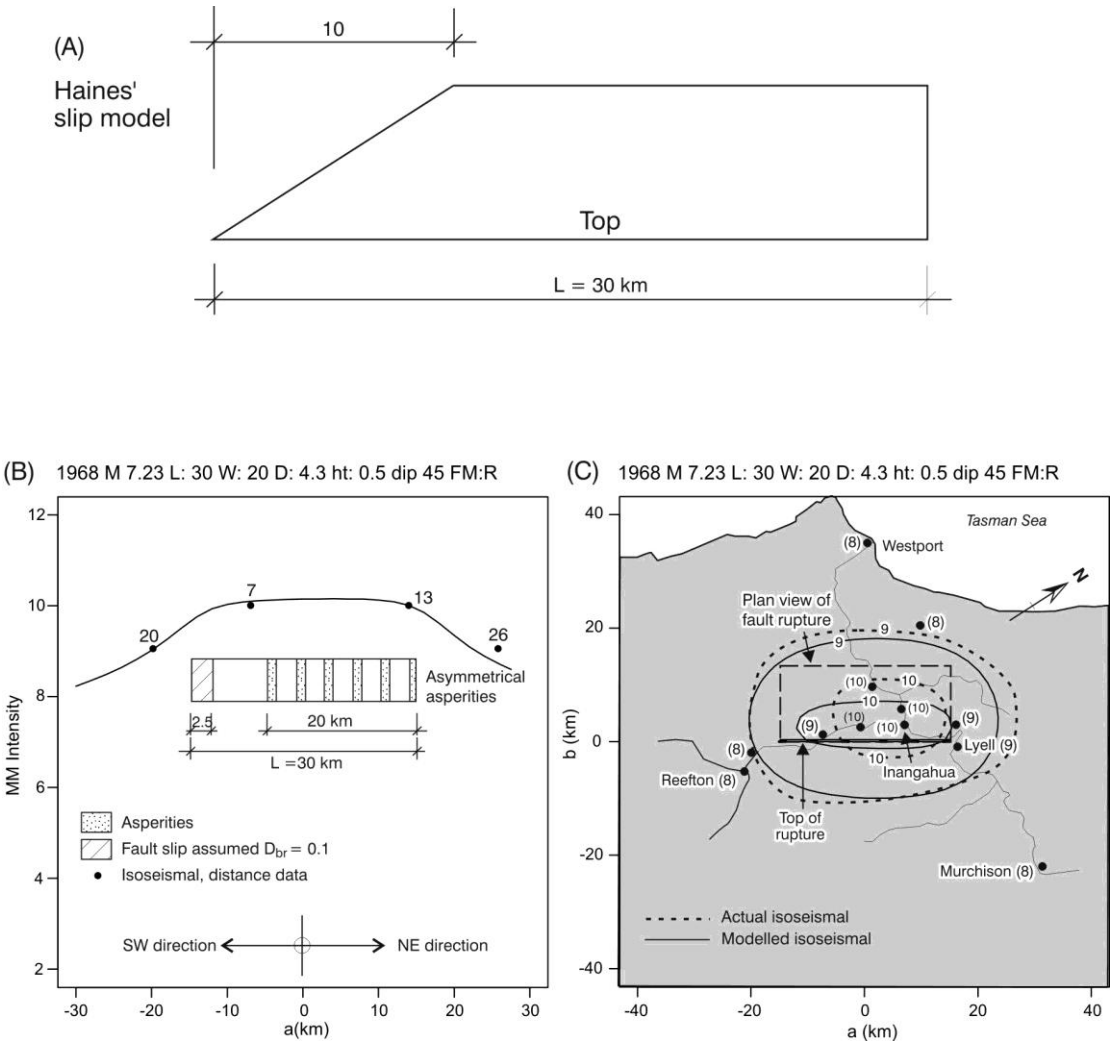

Figure 16: ***Comparison of the MM9 and MM10 isoseismals from the 2-D source model (asymmetrically distributed asperities, A_{ar} = 0.21) vs. actual, for the M_w 7.23 1968 Inangahua earthquake: (A) Plan view of Haines' source and fault slip model (Anderson et al., 1994), (B) Linear scale plot of attenuation in along-strike direction derived with modelling of asperities to approximately simulate Haines' slip assumption shown on (A) above and (C) Map of the actual MM9 and MM10 isoseismals and those modelled as shown on (B) above. (See last sentence of Figure 14 caption).***

Sensitivity to asperity toughness

In the foregoing modelling, the asperities were mostly assigned displacements of 1.83 times the mean displacement of the whole rupture surface, i.e. D_{ar} = 1.83, plus one case where the value of D_{ar} was taken to be 2.2 (Figure 15). The sensitivity of the near-source intensity to a substantially tougher asperity (ie higher D_{ar}) is now examined, adopting the asperity distribution shown on Figure 18A, Case 1, for the 1931 Hawke's Bay earthquake rupture surface. The choice of this distribution was influenced by those estimated for the Kobe (Wald, 1996) and Morgan Hill (Hartzell and Heaton, 1986) earthquakes. As seen on Figure 2, the value of D_{ar} for Morgan Hill earthquake is given by Somerville *et al.* (1999) as 3.4, and is 57 percent larger than for that of the next largest value of D_{ar} of the other nine Californian earthquakes in their data set. For the toughest asperity on Figure 18A, a value of D_{ar} of 4.0 has been adopted. As the mean displacement for this earthquake is 7.11 m, this represents a displacement of 28.4 m on this asperity, which is 3 percent of the area of the rupture.

As seen on Figure 18A, we consider the tough asperity at two depths, 2 km to its top (Case 1) and 10 km deep (Case 2), with a width of 8 km. The general effect of the asymmetrical asperity distributions shown on Figure 16A is to cause the asymmetrical distribution of intensity in the along-strike direction seen on Figure 18B, and the intensity local to asperities 1 and 2 is c. 0.3 units higher than the intensity further along the fault rupture (Figure 18C). This local increase in intensity has been caused by the asperities releasing 44 percent of the total seismic moment released by the whole rupture. In Case 2, where the tough asperity is 10 km rather than 2 km deep, it is seen that the MM intensity is only decreased by c. 0.1 units. The change in intensity is small because moving asperity 2 involves moving only 7.5 percent of the total seismic moment (See also the discussion of the effect of the deepness of asperities on Figure 9).

Influence of dip

The influence of the dip of the fault rupture on the spatial distribution of intensity is illustrated by comparing the inner isoseismals predicted by the 2-D source model of the 1931 Hawke's Bay earthquake assuming two different angles of dip, i.e. 30º and 90º. On 917 it is seen that the change in dip from 90º to 30º moves the MM9 isoseismal 9 km in the down-dip direction, and moves the MM10 isoseismal about 7 km. These changes in location of these isoseismals represent an increase in the intensity of 0.3-0.5 units at down- dip distances of up to about 25 km. The shallower dip causes an increase in the width of the MM10 and MM9 isoseismals, but not for isoseismals of intensity ≤ MM8.

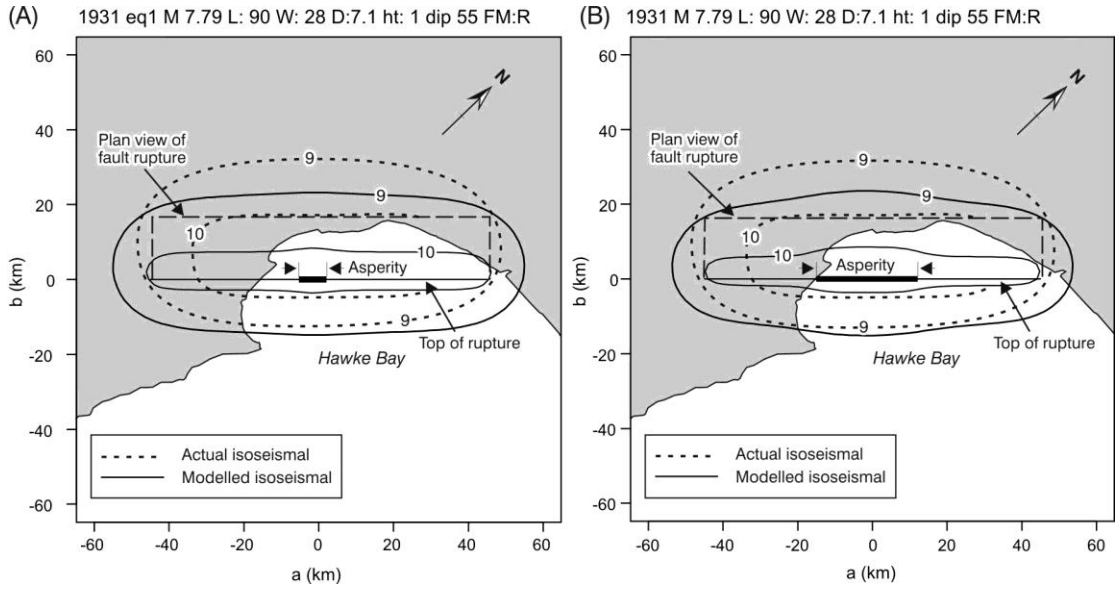

Figure 17: ***Sensitivity to area of asperities: Comparisons of the MM9 and MM10 isoseismals from 2-D source models with evenly spaced asperities having (A) A_{ar} = 0.1 and (B) A_{ar} = 0.3, with the actual isoseismals of the M_w 7.79 1931 Hawke's Bay earthquake. (cf. Figure 14(B)).***

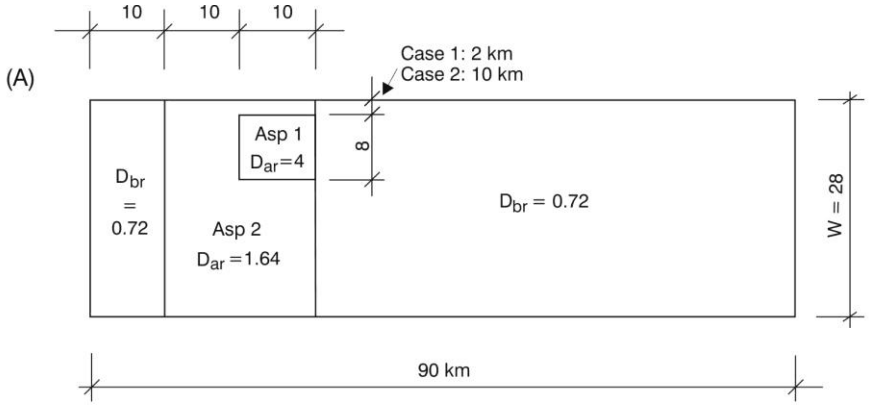

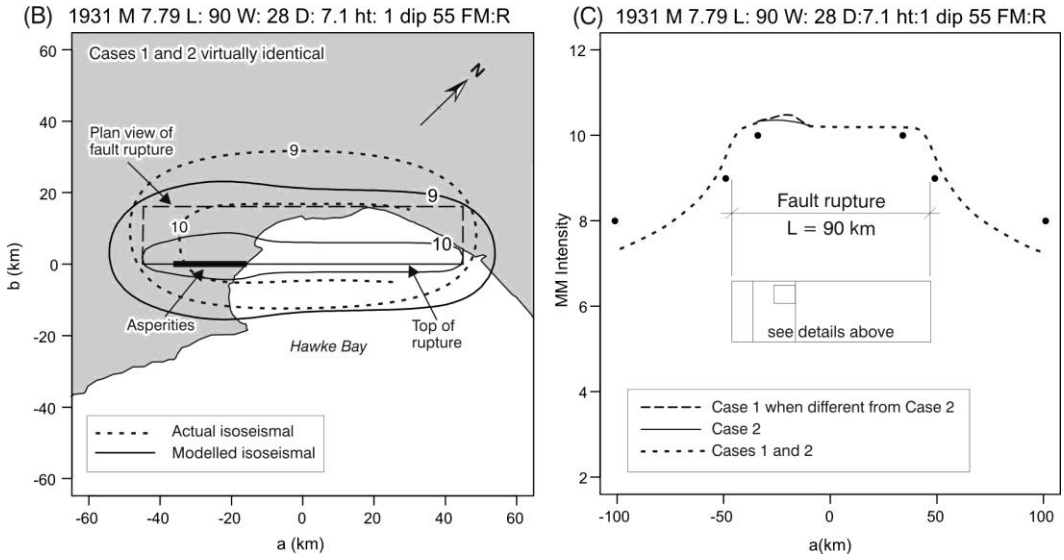

Figure 18: ***Sensitivity to larger displacement on asperities: (A) Asperity model with an intense asperity (partly based on Kobe, Japan, and Morgan Hill, USA, earthquakes) for application on the Hawke's Bay earthquake fault rupture, (B) Map of the actual MM9 and MM10 isoseismals of the M_w 7.79 1931 Hawke's Bay earthquake and those modelled as shown on (A) above (cf. Figure 14B) and (C) Linear plot of intensity along the top of the fault rupture as modelled in (B) above plus data. (cf. Figures 9 and 14(B)).***

Influence of depth to top of rupture

Obviously the near-source intensity is strongly influenced by the depth to the top of the fault rupture, h_t . To quantify this effect for a very large earthquake the intensity was calculated using the 2-D source model for the M_w 8.2 Wairarapa earthquake, with evenly spaced asperities and source parameters as modelled above, except that the dip has been taken as vertical. The along-strike intensity has been plotted to linear scale for h_t = 0, 5 and 8 km on Figure 20. Here it is seen that by changing h_t from zero to 8 km the intensity decreases by one unit from MM10.6 to MM9.6. It is also seen that the local increases in intensity caused by the asperities become negligible when $h_t \approx$ 8km.

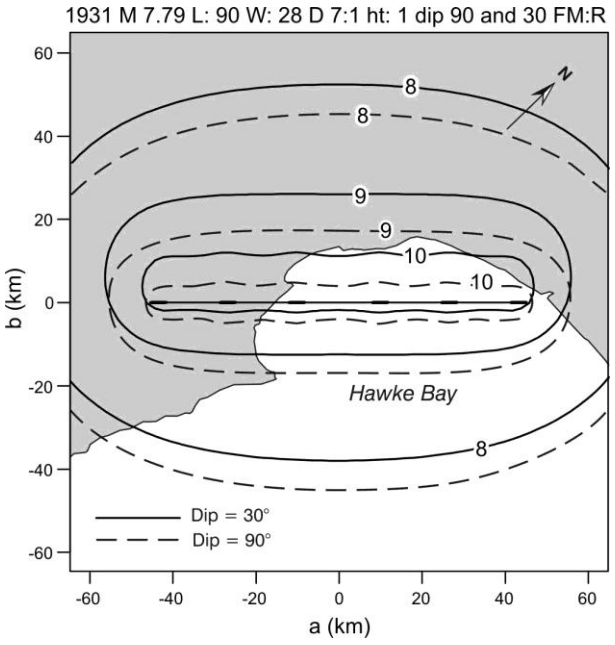

Figure 19: Sensitivity to fault dip, β : Comparisons of the inner isoseismals of the M_w 7.79 1931 Hawke's Bay earthquake, predicted using the 2-D source model assuming dips of 30° and 90°. The models have evenly spaced asperities having A_{ar} = 0.21 and h_t = 1 km in both cases.

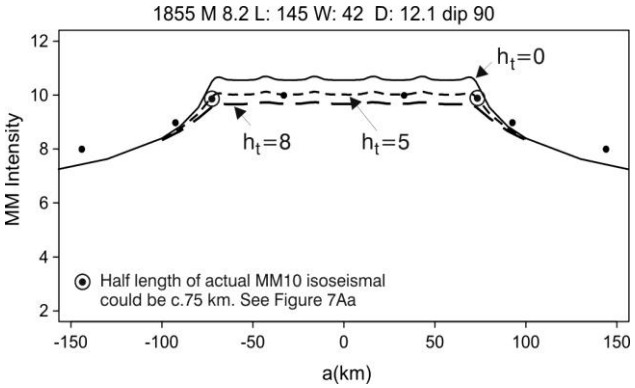

Figure 20: Sensitivity to depth to top of rupture, h_t : Linear scale attenuation plots in the along-strike direction predicted by the 2-D source model, with h_t = 0, 5 and 8 km and evenly spaced asperities having A_{ar} = 0.21, against the a-direction data for the M_w 8.2 1855 Wairarapa earthquake (with dip = 90º). Asperities are as shown on Figure 9.

Influence of rupture width and fault rupture aspect ratio L/W

A simple way of demonstrating the effect of rupture width is to compare the inner isoseismals predicted by the 2-D source model for fault rupture of a given length having two alternative widths. For this purpose we took the M_w 8.2 Wairarapa earthquake which has rupture length 145 km and a biplanar width W = 42 km, and also modelled the case where W was reduced (considerably) to 15 km and M_w consequently became 7.9. The inner isoseismals for these two events are compared on Figure 21, where it is seen that the innermost isoseismals (MM10) are nearly identical for the two cases. For a fault rupture of substantial length such as this, noticeable reduction in the maximum intensity will occur when the width reduces to 10-12 km. With increasing distance from the fault, the intensities from the narrower rupture become increasingly lower than those caused by the larger magnitude event. For example, on Figure 21 at distances down-dip of b = +5 and +100 km, the intensities for the W = 15 km event are 0.1 and 0.4 less respectively than those for the W = 42 km event.

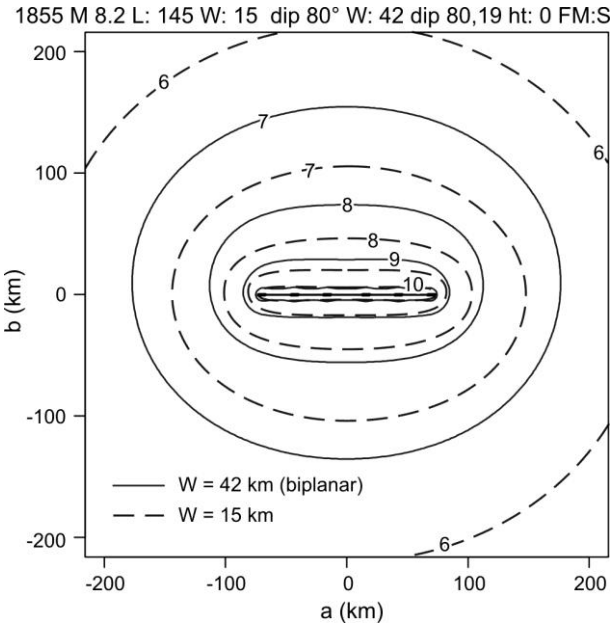

Figure 21: Sensitivity to rupture width, W: Comparison of the inner isoseismals predicted by the new models for the M_w 8.2 1855 Wairarapa earthquake modelled with A_{ar} = 0.21, and evenly spaced asperities, with rupture widths D = 42 km (biplanar source) and 15 km (2-D source). Note the very small differences in the near fault intensities caused by omitting the bottom 27 km width of the fault rupture; the MM10 isoseismals are virtually coincident.

In addition the near-source intensities were calculated for two near-surface h_t = 1 km earthquakes of M_w 7.0 and fault ruptures of the same area (360 km^2) with aspect ratios of L/W = 18/20 = 0.9 and 36/10 = 3.6. The intensity above the centre of the fault rupture, I_0, was found to be almost the same in both cases, i.e. MM10.0 and MM9.9 respectively. This is explained by the fact that in the first case, where W = 20 km, the lower half of the fault rupture contributes little to the near-source intensities as was seen to be the case illustrated on Figure 21. Similar results were obtained when comparing the

near-source intensities of two events of M_w 6.6 with L/W = 14/12 and 19/8.8. Thus it appears that the maximum intensity I_0 is barely influenced by a wide range of realistic aspect ratios of the fault rupture. It is noted that the effect of aspect ratio on intensity decreases with increasing h_t.

Situations where the predictions of the 2-D or 3-D source model may be of particular interest

The 2-D (and 3-D) source model was developed mainly to predict near-source intensities (MM9 and MM10) of large near surface earthquakes, in particular to directly model the effects of a 2-D or 3-D source including the effects of asperities on the rupture surface, neither of which are incorporated into conventional attenuation models such as that of Dowrick & Rhoades (2005) and conventional strong motion attenuation models (e.g. McVerry *et al.* (2006). In addition to the various effects discussed above, it will be helpful to know in which situations the 2-D or 3-D source model will give more reliable predictions of the spatial distribution of intensities near the source.

First we note that the shape and extent of the MM10 isoseismal are influenced mainly by the length of the fault rupture (L) and the depth to the top of the rupture (h_t). In addition the asymmetrical location of the MM9 and MM10 isoseismals becomes marked for earthquakes of larger L and dip < 60º. These features are clearly shown on Figures 7A, B and C and Figure 8 (where the 2-D and 3-D source models fit most of the MM9 and MM10 data better than does the 2005 model (Table 5)). On Figure 22 are plotted the L,h_t pairs of 10 earthquakes from our data set to examine the effect of depth more widely, for five of these events we have considered them as occurring at a range of values of h_t, e.g. for the largest event, 1855 M_w8.2, L=145 km, values of h_t of 0, 8 and 10 km were used. Considering the attenuation plots of each of the above cases, the fits of the MM9 and MM10 isoseismals predicted by the 2-D and 3-D source models and the D&R (2005) model were compared. Figure 5Ba shows such a plot for the 1901 event, with L = 24 km and h_t = 4 km, where the 2-D model fits the MM9 data marginally better in the *a*-direction and substantially better in the *b*-direction. Figure 5Aa for the 1929 Arthur's Pass event, with L = 30 km and h_t = 0 km, shows the length of the modelled zone of maximum intensity (almost MM10) to be greater for the 2-D source model than that for the D&R (2005) model, and the 2-D source model fits the MM9 data better for both the *a*-and *b*-directions. Thus part of the threshold for divergence between the two models lies between the L,h_t pairs of these two events, and the threshold extends to events with h_t down to about 10 km for L = 145 km (see Figure 22). In addition we know (Dowrick and Rhoades (in prep.) that the 2-D source model is equally valid for earthquakes with L > 145 km, such as those on segments of the Alpine fault where L ranges up to > 400 km.

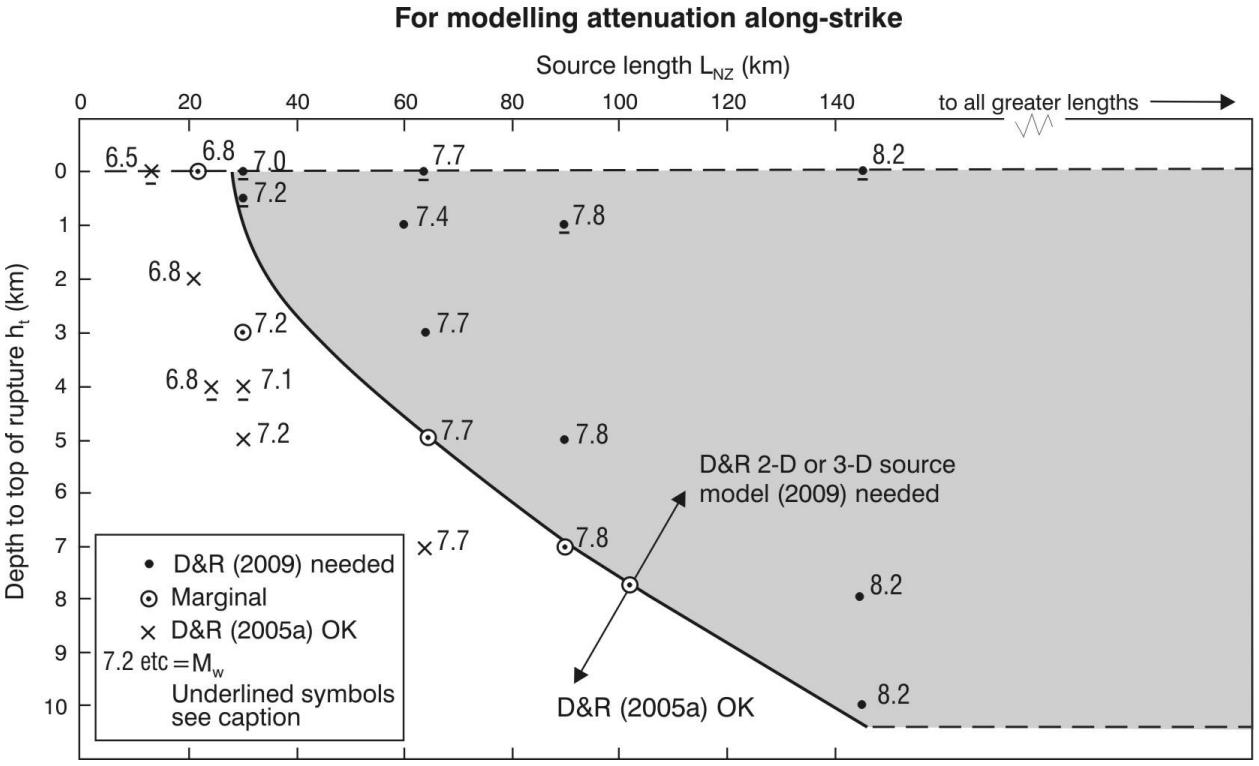

Figure 22: Plot of rupture length (L) vs. depth to top of rupture (h_t) showing the zone of New Zealand earthquakes with L, h_t pairs where the 2-D source model predicts longer and more reliable lengths and more reliable widths for the innermost (ie MM9 and MM10) isoseismals than does the attenuation model of Dowrick & Rhoades (2005). The magnitude is also given of each event plotted.

6 CONCLUSIONS

1. The new attenuation model for MM intensities incorporating 2-D and biplanar sources predicts near-source isoseismals for near surface New Zealand fault ruptures longer than about 35 km, which are substantially longer than those of Dowrick & Rhoades (2005), and are more consistent with the near-source spatial distributions of strong motion models. The lengths of the predicted MM9 isoseismals are close to those of the actual MM9 isoseismals, while the lengths of the predicted MM10

isoseismals are consistent with those data which are robust.

2. For large earthquakes with dip < 60º, the 2-D/3-D models locate the MM9 and MM10 isoseismals in the strike-normal direction substantially better than does the D&R (2005) model.

3. The new attenuation model predicts isoseismal dimensions in the far field (MM8 and less) which are consistent with the data and are closely similar to those of the model of D&R (2005).

4. For shallow earthquake ruptures of length ≥ c. 24 km, attenuation in the along-strike direction incorporates a (new) reverse curvature feature, which is seen to extend from near the end of the fault rupture out to about intensity MM4, i.e. over a distance of up to about 500 km. The reverse curvature is necessary for providing a transition between the intensity plateau along to the end of the fault rupture and the far-field attenuation line.

5. The concept of *seismic source intensity* is introduced, and used to verify the phenomenon of reverse curvature of the along-strike attenuation curve mentioned above.

6. Although the new model has only four free parameters and has no fitted parameters for focal mechanism, its goodness of fit is comparable to the models of D&R (2005), and its fit to the small number of available near-source data near-source data is good. It has no obvious biases with respect to isoseismal distance, or earthquakes of different magnitudes, fault dimensions, or focal mechanisms. In the absence of isoseismal data on large earthquakes with normal focal mechanisms the current model is only verified for use on strike-slip and reverse events.

7. The residuals for the 20 data points of the MM9 and MM10 isoseismals of the six largest earthquakes (M_w 6.95 -8.2) with MM9 isoseismals are listed in Table 6. The mean value of these residuals is -0.005 units of intensity, showing that the new models fit the near-source data of the largest earthquakes very well.

8. The size and shape of the predicted inner isoseismals are sensitive to the parameters L, W (< c. 15), D, h_t, β and d. MM10 isoseismals may or may not enclose the top of the rupture, while MM9 isoseismals enclose the top of the rupture if $M_w \geq 7, L$ > 20 km and $h_t \leq$ c. 2 km. In contrast, varying the locations of the asperities on the rupture surface was found to make little difference to the spatial distribution of intensity, except near the source of large near-surface ruptures. The greatest increase in intensity (ΔI = 0.3) due to asperities was caused by the combination of two asperities which together released 44 percent of the total seismic energy of the earthquake being modelled (Figure 18). Small variations of this sort would not be detectable in field observations of intensities, which are assigned only in full units of intensity.

9. Patterns of distribution of displacement on the rupture surface are modestly influential on the size and shape of the MM10 isoseismal. For any given event, as the asperities commonly contribute about 30-50 percent of the seismic moment, the non-asperity area generally contributes 50-70 percent of the moment. This means that the non-asperity area is at least as influential as the asperities in dictating the size and shape of the isoseismals.

10. It follows from the previous two conclusions that source modelling using no asperities is satisfactory for most purposes.

11. In the along-strike direction, the centres of all of the predicted isoseismals are coincident with the centre of the moment release of the rupture surface.

12. Only those parts of localised asperities within a few kilometres of the surface result in predicted local increases in intensity.

13. The depth to the top of the rupture, h_t, strongly affects the value of the maximum intensity. For example, for an event of $M_w 7.8$, values of h_t = 0 and 8 km result in maximum intensities of 10.6 and 9.6 respectively.

14. The aspect ratios L/W of the fault ruptures of near-surface earthquakes barely influences the maximum intensity I_0. This occurs because the lower parts of wide faults contribute more to far field than to near-source intensities.

15. The 2-D and 3-D source models will give more reliable predictions of the near-source spatial distribution of intensities (MM9 and MM10) than does the model of D&R (2005) for New Zealand earthquakes in which the rupture length is greater than that defined by a curve through (L, h_t) pairs of approximately (28 km, 0 km) to (145 km, 10 km). The 2-D source model is also valid for all events of L > 145 km.

16. The new attenuation model is a widely applicable tool that has been shown capable of modelling spatial distributions of MM intensity in the near and far fields, for crustal New Zealand earthquakes with rupture lengths of up to 145 km. It applies also to very long sources (e.g. the Alpine fault) and any dip angle. The methodology is capable of being extended to subduction interface events, although it is likely that the coefficients of Equation 3 will need to be refitted for these events. The latter two types of event are out of the range of applicability of the models of D&R (2005).

7 ACKNOWLEDGEMENTS

The authors wish to thank Graeme McVerry, John Zhao and Rafael Benites for their helpful in-house reviews. We are also grateful to Euan Smith for his constructive external review.

8 REFERENCES

Anderson, H., Webb, T., and Jackson, J. (1993). Focal mechanisms of large earthquakes in the South Island of New Zealand: implications for the accommodation of pacific- Australia plate motion. *Geophysics Journal International* **113**: 1032-1054.

Anderson, H., Beanland, S., Blick, G., Darby, D., Downes, G., Haines, J., Jackson, J., Robinson, R. and Webb, T. (1994). The 1968 May 23 Inangahua, New Zealand earthquake: an integrated geological, geodetic, and seismological source model. *New Zealand Journal of Geology and Geophysics* **37**: 59-86.

Darby, D.J. and Beanland, S. (1992). Possible source models for the 1855 Wairarapa earthquake, New Zealand. *Journal of Geophysical Research* **97**(B9): 12,375-12,389.

Doser, D.L. and Webb, T.H. (2003). Source parameters of large historic (1917-1961) earthquakes, North Island, New Zealand. *Geophysical Journal International* **152**: 795-832.

Doser, D.L., Webb, T.H. and Maunder, D.E. (1999). Source parameters of large historic (1918-1962) earthquakes, South Island, New Zealand. *Geophysical Journal International* **139**: 769-794.

Downes, G.A. and Dowrick, D.J. (in prep) *Atlas of isoseismals maps of New Zealand earthquakes*. 2nd Edition. GNS Science, Lower Hutt, New Zealand.

Dowrick, D.J. (1994). Damage and intensities in the magnitude 7.8 1929 Murchison, New Zealand, earthquake. *Bulletin of the New Zealand National Society for Earthquake Engineering* **27**(3): 190-204.

Dowrick, D.J. and Rhoades, D.A. (2004). Relations between earthquake magnitude and fault rupture dimensions: How regionally variable are they? *Bulletin of the Seismological Society of America* **94**(3): 776-788.

Dowrick, D.J. and Rhoades, D.A. (2005). Revised models for attenuation of Modified Mercalli intensity in New Zealand earthquakes. *Bulletin of the New Zealand Society for Earthquake Engineering* **38**(4): 185-214.

Dowrick, D.J. and Rhoades, D.A. (in prep.) Spatial distribution of ground shaking in characteristic earthquakes on the Wellington and Alpine faults, New Zealand, estimated from a distributed-source model.

Dowrick, D.J., Rhoades, D.A. and Davenport, P.N. (2001). Damage ratios for domestic property in the 1968 Inangahua, New Zealand, earthquake. *Bulletin of the New Zealand Society for Earthquake Engineering* **34**(3): 191-213.

Dowrick, D.J., Hancox, G.T., Perrin, N.D. and Dellow, G.A. (2008). The Modified Mercalli intensity scale – Revisions arising from New Zealand experience. *Bulletin of the New Zealand Society for Earthquake Engineering*, **41**(4): 193-205.

Haines, A.J. and Darby, D.J. (1987). Preliminary dislocation models for the 1931 Hawke's Bay and 1932 Wairoa earthquakes. New Zealand Geological Survey Report EDS 114.

Hancox, G.T., Perrin, N.D. and Dellow, G.D. (1997). Earthquake-induced landsliding in New Zealand and implications for MM intensity and seismic hazard assessment. Institute of Geological Sciences, Client Report 43601B, prepared for the Earthquake Commission Research Foundation.

Hanks, T.C. and Kanamori, H. (1979). Moment magnitude scale. *Journal of Geophysical Research* **84** (B5): 2348–2350.

Hartzell, S.H. and Heaton, T.H. (1986). Rupture history of the Morgan Hill, California, earthquake from the inversion of strong motion records. *Bulletin of the Seismological Society of America* **76**: 649-674.

Kendall, M. and Stuart, A. (1977). *The Advanced Theory of Statistics: Volume 1*, Fourth Edition, McMillan, New York, 472pp.

McVerry, G.H., Zhao, J.X., Abrahamson, N.A. and Somerville, P.G. (2006). New Zealand acceleration response spectrum attenuation relations for crustal and subduction zone earthquakes. *Bulletin of the New Zealand Society for earthquake Engineering* **39**(1): 1-58.

Smith, W.D. (1995). A procedure for modelling near-field earthquake intensities. *Bulletin of the New Zealand National Society for Earthquake Engineering* **28**(3): 218-223.

Somerville, P.G., Irakura, K., Graves, R., Sawada, S., Wald, D., Abrahamson, N., Iwasaki, Y., Kagawa, T., Smith, N. and Kowada, A. (1999). Characterizing earthquake slip models for the prediction of strong ground motion. *Seismological Research Letters* **70**: 59-80.

Wald, D.J. (1996). Slip history of the 1995 Kobe, Japan, earthquake determined from strong-motion, teleseismic, and geodetic data. *Journal of Physics of the Earth* **44**: 489-503.

Webb, T.H. and Anderson, H. (1998). Focal mechanisms of large earthquakes in the North Island of New Zealand: slip partitioning at an oblique active margin. *Geophysical Journal International* **134**: 40-86.

APPENDIX 1: Derivation of formula for k

Let $I(n; M_0 / n; R_1, \cdots, R_n)$ represent the intensity resulting from n sub-events each of seismic moment M_0/n at n distances R_1, …, R_n, which may be the same or different. In this notation, $I(1; M_0, R)$ is the intensity resulting from a single earthquake of moment M_0 at distance R.

From the concept of effective distance, we have

$$I(n; \frac{M_0}{n}; R_1, \cdots, R_n) = I(1; M_0; R_{eff}) \quad \text{(A1)}$$

where R_{eff} is defined by

$$\frac{n}{R_{eff}^{\ k}} = \sum_{i=1}^{n} \frac{1}{R_i^{\ k}} \ . \quad \text{(A2)}$$

The exponent k is determined below.

Consider the intensity due to a single earthquake of seismic moment M_0/n at distance R. This is conceptually equivalent to an earthquake of magnitude M_0 which has one sub-event of moment M_0/n at distance R together with n-1 sub-events of the same seismic moment at infinite distance. Such a limiting scenario cannot be realised in practice. But it is approximately realised when a very long source is subdivided into a few notional elements and a site of interest is close to one element but far away from the others. By Equation A2, the effective distance for the event of seismic moment M_0 equivalent to these n sub-events is $(nR^k)^{1/k}$, or $Rn^{1/k}$. Therefore we have

$$I(1; \frac{M_0}{n}; R) = I(n; \frac{M_0}{n}; R_1 = R; R_i = \infty, i = 2, \cdots, n) = I(1; M_0; Rn^{1/k}) . \quad \text{(A3)}$$

If magnitude M_{wn} corresponds to moment M_0/n and magnitude M_w corresponds to moment M_0, then from the definition of the moment magnitude scale (Hanks and Kanamori, 1979), for a constant c independent of magnitude, we have

$$M_w = 2/3 \log M_0 + c$$

and

$$M_{wn} = 2/3 \log \frac{M_0}{n} + c = M_w - \frac{2}{3} \log n . \quad \text{(A4)}$$

Since the model for a single point source is given by

$$I = A_1 + A_2 M_w + A_3 \log R + A_4 h_c ,$$

Equation A3 leads to

$$A_2 M_{wn} + A_3 \log R = A_2 M_w + A_3 \log(Rn^{1/k}).$$

Applying Equation A4, we then have

$$A_2 M_w - \frac{2}{3} A_2 \log n + A_3 \log R = A_2 M_w + A_3 \log R + \frac{A_3}{k} \log n . \quad \text{(A5)}$$

Solving (A5) for k, we obtain $k = -1.5 A_3 / A_2$.

APPENDIX 2: Trade-off between seismic moment and distance

Consider a small sub-event with seismic moment M_a at distance R, where $M_a = \alpha M_b$. To any desired accuracy, the real number α can be approximated by a rational number m/n, where m and n are integers. Then we have

$$I(1, M_a; R) \approx I(1, mM_b / n; R) = I(1, mM_b; Rn^{1/k}) = I(1, M_b; R(n/m)^{1/k} \approx I(1, M_b; R\alpha^{-1/k}) ,$$

where the second equality is by a straightforward application of Equation A3, and the third by a reverse application of Equation A3. Hence the seismic moment M_a at distance R is equivalent to M_b at distance $R\alpha^{-1/k}$.